EXPERIMENTAL EFFECTS OF THERMAL CYCLING ON TITANITE MORPHOLOGY AND GROWTH

Tyler David Wickland

A thesis submitted to the faculty at the University of North Carolina at Chapel Hill in partial fulfillment of the requirements for the degree of Master of Science in the Department of Geological Sciences.

Chapel Hill
2016

Approved by:

Allen F. Glazner

Drew S. Coleman

Ryan D. Mills

ABSTRACT

Tyler David Wickland: Survival of the fattest: titanite growth during thermal cycling experiments
(Under the direction of Allen F. Glazner)

One-atmosphere, thermal cycling experiments on titanite in silicic melt provide growth rates, crystal number densities, and textural morphologies in order to better understand crystal populations in thermally oscillating magmatic environments. Titanite commonly occurs as relatively large, euhedral crystals in granitoid rocks with complex oscillatory zoning patterns that suggest a convoluted thermal history. Thermal cycling experiments demonstrate that titanite populations are coarsened by the combination of size-dependent precipitation and dissolution processes. Both the amplitude and the number of cycles have a larger positive correlation to crystal size than the period of the cycle. Titanite populations reach new textural equilibria of larger, fewer crystals when compared to static temperature crystal growth. Thermal cycling is ubiquitous in forming igneous rocks and affects the classical interpretations of crystal size distributions to include more dynamic and complex thermal processes.

ACKNOWLEDGEMENTS

I would like to thank my advisor, Dr. Allen Glazner for his invaluable assistance through all steps this project. Thank you to my thesis committee members, Drew Coleman and Ryan Mills, for in-depth review of my thesis. This work would not be possible without funding from the NSF grant 1250505 and the Martin Fund. I greatly appreciated assistance from Rebecca Rodd with creating figures. Finally, I would like to commemorate my uncle, Dr. Thomas Hooyer, who recently passed away. He was a great inspiration to me while working on this project.

TABLE OF CONTENTS

LIST OF TABLES

LIST OF FIGURES

LIST OF ABBREVIATIONS AND SYMBOLS

A	crystal area
α	amplitude
ab	albite
atm	atmosphere
BSE	backscattered electron
CSD	crystal size distribution
CN	communicating neighbors
°C	degrees Celsius
2D/3D	two or three dimensions
Φ	crystal area fraction
G	growth rate
h	hour
kV	kilovolts
min	minute
mm	millimeter
µm	micrometer
N_A	crystal area density
N_V	crystal volume density
nA	nanoamps
REE	rare earth element
S_N	characteristic size
T	temperature

$\overline{T}$	mean temperature
t	time
τ	period
ttn	titanite
wt%	weight percent
XRF	X-ray fluorescence

INTRODUCTION

Igneous textures

Crystal textures in igneous rocks are indicative of the magmatic processes and environments under which they grew (e.g., Lofgren, 1980; Hersum and Marsh, 2007). Textures are controlled by the interplay of nucleation, growth, and their thermal history (Carmichael et al., 1974; Lofgren, 1974; Donaldson, 1976). Historically, textural analysis has lacked the quantitative approach that advanced the related field of geochemistry (Jerram and Davidson, 2007). In a series of papers, Marsh and others made great strides to quantify textures, particularly by the use of crystal size distributions (CSDs) in silicate melts (Cashman and Marsh, 1988; Marsh, 1988). Cashman and Marsh applied CSD analysis to samples from a crystallizing basaltic lava pool and quantified nucleation and growth during cooling. Textural analyses of igneous rocks often oversimplify controlling factors such as Ostwald ripening, nucleation, and thermal conditions for pervasively dynamic crystal-melt systems (Pupier et al., 2008; Schiavi et al., 2009). Linking crystallization factors of silicate magmas and their resultant textures is important because crystal growth processes that govern the textures of natural magma systems are not well understood.

Crystal growth

Ostwald (1896) demonstrated that larger crystals can coarsen at the expense of smaller ones under isothermal conditions and constant crystal volumes caused by the reduction of energy at solid-liquid interfaces (Voorhees, 1985). However, this process can take 10^5 - 10^9 years to

affect larger crystal sizes (e.g. Nemchin et al., 2001) because only crystals close to their critical nucleation radius (≤ 1-5 μm) are ripened (Cabane, 2001; 2005; Simakin and Bindeman, 2008). Ostwald ripening may be viable in static temperature conditions, but conditions during the crystallization of a melt are subject to changes in temperature (e.g., Huppert and Sparks, 1988; Harper et al., 2004). Growth processes for crystallization under dynamic conditions are different from those under static or constant cooling conditions.

Disequilibrium crystallization occurs when conditions of crystallization change rapidly (Loomis, 1982). For example, crystallization during temperature oscillations keeps crystals in a state of disequilibrium because conditions are constantly changing. Crystal coarsening associated with temperature instabilities has previously been studied in materials science (Hintzmann and Müller-Vogt., 1969; Scheel and Elwell, 1972), food science (Donhowe and Hartel, 1996), and in magma systems (Lofgren, 1974; Paque et al, 2000; Zieg and Lofgren, 2006; Mills et al., 2011). Wu et al. (2016) linked temperature oscillations to controlling the size and quality of Fe_2O_3 polymorphs in solution, further highlighting the use of dissolution-recrystallization processes across many fields of study.

Thermal cycling

Temperature fluctuations are likely ubiquitous in magmatic settings and can profoundly affect the textures and CSDs of igneous rocks and igneous analog materials (Marsh, 1988; Mills et al., 2011; Mills and Glazner, 2013). Simakin and Bindeman (2008) developed a theoretical model for precipitation-dissolution events in igneous systems, factoring in size-dependent treatment of crystal populations in thermally oscillating regimes. Mills et al. (2011) favored this model by coarsening ammonium thiocyanate (analog magma system) during thermal cycling

experiments. These experiments revealed that textural coarsening during crystallization of silicate melts could be significantly influenced by oscillating temperatures.

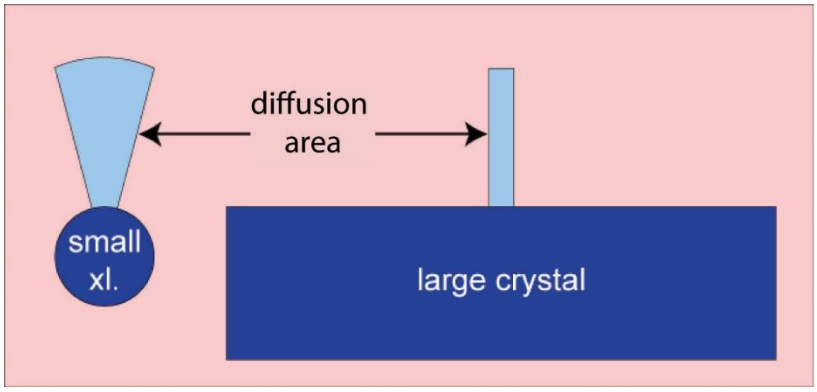

Figure 1. Smaller crystals, modeled as spherical, are exposed to larger amounts of melt than larger crystals. They are more susceptible to dissolution processes where greater amounts of material may diffuse into larger melt areas. Even with similar crystal shapes dissolution is inversely proportional to size due to the curvature of a dissolving surface and related diffusion flux (Simakin and Bindeman, 2008).

Mills and Glazner (2013) carried out thermal cycling experiments on plagioclase and olivine in a basaltic melt, revealing that thermal cycling significantly reduced the number of crystals per unit area (number density) and enhanced growth. Plagioclase grew 60% faster in cycled experiments compared to constant temperature experiments. They supported Simakin and Bindeman's (2008) proposal that crystal dissolution is inversely proportional to size due to the curvature of the surface of a dissolving crystal, exposing larger crystal areas (in 2D) to the surrounding melt (Fig. 1).

The growth effects of thermal cycling are not well understood because of the interrelationships between amplitude, period, time and temperature of oscillations (Simakin and Bindeman, 2008). Crystal growth is positively correlated with the amplitude of a temperature cycle and with the period of a cycle except when the period is exceedingly short. For example, Mills and Glazner (2013) suggested that at less than 10 minute periods, diffusion distances of crystal solute did not redistribute non-touching crystals significantly. In their experiments,

nucleation is observed to be suppressed during thermal cycling and is limited to existing crystal sites by the reduction of crystal number densities. This study will use several measures of textural analysis to examine separately the effects of amplitude, period, and mean temperature on crystal growth and nucleation.

CSDs

CSDs are commonly lognormal for igneous rocks (e.g. Eberl et al. 2002) and are used to describe and interpret igneous textures (Cashman and Marsh, 1988; Higgins and Roberge, 2003; Pupier et al., 2008; Higgins, 2011). CSD analysis quantifies textures using the relationship between cumulative numbers of particles and their sizes (Fig. 2). CSDs are typically described by the natural log of the volumetric number density plotted against the crystal size. In cases where discrete 3D crystal sizes are unknown, volume number densities for a size interval are divided by the length of that size interval (Higgins, 2006). Blundy and Cashman (2008) outlined the use of CSD slopes to link population densities and crystal sizes to magmatic conditions. Higgins (1998; 2000; 2006) expanded the field of CSD analytics, creating the software *CSDcorrections* (Higgins, 2000), which allows for physical parameters like crystal areas and shapes in 2D sections to be extrapolated to 3D volumetric measurements (stereology).

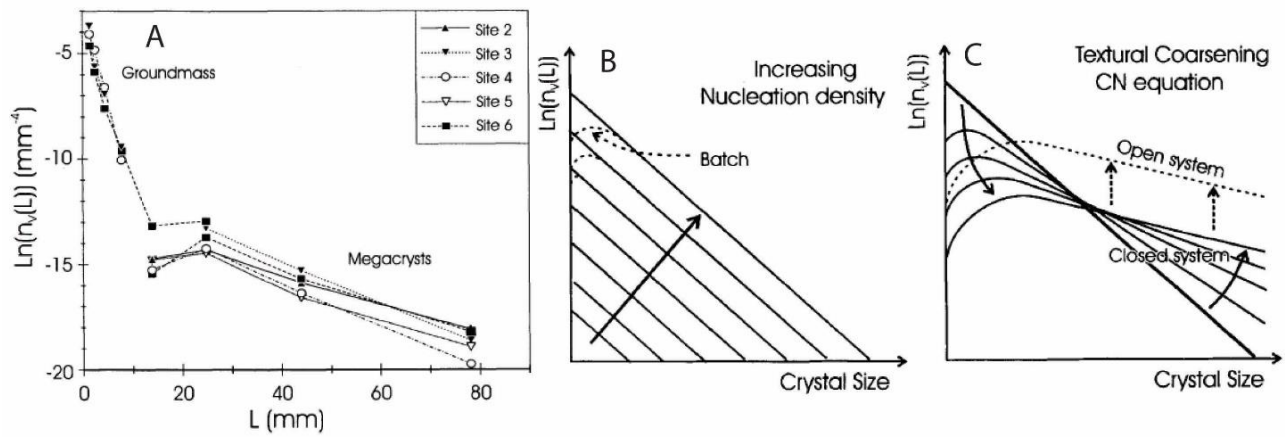

Figure 2. a) CSD of K-feldspar from Cathedral Peak Granodiorite, California, (Higgins, 1999) showing separation of slopes between groundmass and megacryst populations. Modeled CSDs by Higgins (1999) for b) linear increasing nucleation density (Marsh, 1988) and c) textural coarsening using CN equation.

Higgins (1998; 1999) recognized that coarsened crystal populations develop particular CSD slopes that could be modeled with the communicating neighbors (CN) theory. CN theory assumes that crystals coarsen, producing lower slopes on CSD plots, by growth rates controlled characteristically by each crystal, independent of size (i.e. growth dispersion) (Higgins, 1998). Higgins (1998; 1999; 2002; 2006) modeled coarsening CSDs from many igneous suites as diffusion controlled with the CN theory (Fig. 2c). Igneous textures commonly result in lognormal CSDs, which are hard to justify when assuming growth independent of size because that would require prolonged and variable nucleation (Eberl et al., 2002).

Eberl et al. (2002) questioned the popular model for interpreting growth from the slope of a CSD, arguing that linear, or size independent growth is an inaccurate assumption because size variation would be too dependent on variable nucleation rates that do not match experimental nucleation behavior. A better assumption is to treat growth as dependent on size, which more appropriately explains common lognormal CSDs as variations in crystal growth rather than nucleation. Mills and Glazner (2013) modeled crystal coarsening from thermal cycling as size dependent but did not observe log-linear relationships with size in their CSD analyses.

Nevertheless, CSDs are used qualitatively to interpret crystallization histories because CSDs are dependent on the conditions that formed them (Eberl et al., 2001).

Titanite

Titanite is a common accessory mineral in many plutonic rocks, comprising up to 1 wt% of the whole rock (Gromet and Silver, 1983; Bateman and Chappell, 1979). Titanite can be used as a geothermometer (e.g. Cherniak, 2006) and thermobarometer (e.g. Hayden et al., 2008) by measuring Zr diffusion zoning. Titanite incorporates significant quantities of U, Th, rare earth elements (REE), and high field strength elements into its lattice. U incorporation makes titanite useful for U-Pb dating (e.g. Samperton et al., 2015).

In silicic granitoids, titanite is euhedral and is relatively large (up to 1 cm) compared to other accessory minerals (e.g. Glazner et al., 2008; Coleman et al., 2012). These characteristics are classically interpreted as a sign that titanite formed early during crystallization, permitted by unimpeded growth in high melt fractions. However, titanite is also interpreted as late crystallizing (i.e., when uneruptible melt fractions, <50 %, are present) based on the lack of volcanic rocks with U-shaped REE patterns formed due to titanite's affinity for middle REEs (Colombini et al., 2011). Comparing REEs in titanite to residual melts could elucidate the relationship between felsic volcanic and plutonic rocks and has major implications for how high-silica rhyolites relate to plutonic roots in crustal igneous systems (Bachmann and Bergantz, 2008; Glazner et al., 2008).

Timing of titanite formation in silicic magmas thus remains enigmatic. Complex oscillatory and sector zoning further complicate the uncertain growth history of titanite (Paterson and Stephens, 1992; Bauer, 2015). Titanite's typical euhedral form contradicts chemical evidence for late-stage crystallization (e.g. Coleman et al. 2012), and thermal cycling affects

crystal morphology (e.g., Wu et al., 2016). Thus, titanite is well-suited for investigations of thermal cycling effects on crystal growth and texture.

One-atmosphere experiments

In the following two lines of experimentation at 1-atm, titanite crystals were monitored for changes in size and shape during thermal cycling:

1) Experiments held at constant mean temperature ($\overline{T}$) and period (τ) while amplitude (α) was varied 5-20 °C (Fig. 3a; Table 1). Varied-amplitude experiments are compared to static experiments at time intervals from 2 to 120-h (Fig. 3a).
2) Experiments held at constant time (t) and amplitude while the period was varied 24-72 minutes at three $\overline{T}$ that are 10°C apart (Fig. 3b; Table 1). The highest $\overline{T}$ thermal cycle brings the maximum temperature (up-T portion of cycle) within 1°C of the experimentally determined liquidus (Fig. 3b).

Table 1. Experimental notations and abbreviations

	Amplitude experiments	Period Experiments
Notation	α	τ
Starting material	oxides	minerals
Amplitude (°C)	5 - 20	15
Period (min)	24	24-72
$\overline{T}$ (°C)	1280	1265, 1275, 1285

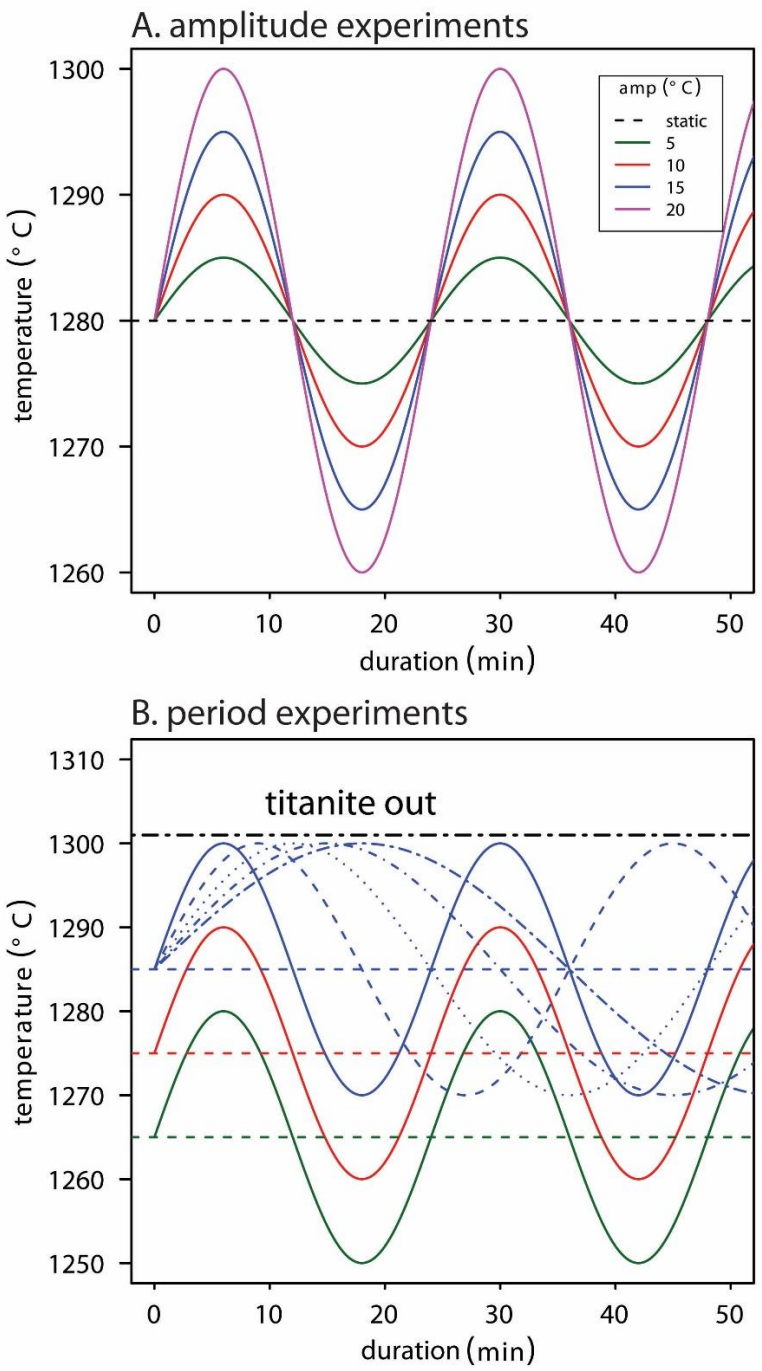

Figure 3. Experimental T-t path for a) α experiments from 5 to 20°C with a constant $\overline{T}$ (1280±1°C) and 24 min τ. Experiments are quenched around 2, 8, 20, 50 and 100-h intervals to construct time series for each α investigated. The system liquidus for α experiments synthetic starting material is 1330±1°C. b) Varied period experiments from 24 to 72 min with constant α 15°C and 50-h duration at three $\overline{T}$'s 1265, 1275, and 1285°C. $\overline{T}$ are 0, 10 and 20°C from the titanite out dashed black line which represents the liquidus of the system (1300±1°C). Variable periods are only shown schematically for one $\overline{T}$ (1285°C) but are carried out for all $\overline{T}$, except for τ 36 and 60 min at $\overline{T}$ 1265°C. Dashed lines at the $\overline{T}$ represent static runs for both α and τ experiment series.

METHODS

Starting materials

Starting materials were chosen for the titanite-albite system because albite has a relatively low melting point (1105°C) compared to titanite (1380°C), allowing titanite crystals to crystallize at relatively low temperatures (Fig. 4). Prince (1943) outlined this eutectic-like pseudo-binary system in which titanite crystals are stable below 1300°C at 50 wt% of each component ($ttn_{50}ab_{50}$; Fig. 4). Experiments were run at $ttn_{50}ab_{50}$ and $\overline{T}$ 1280°C to ensure the stability of titanite and ample melt fractions to ease kinetic restraints on crystallization.

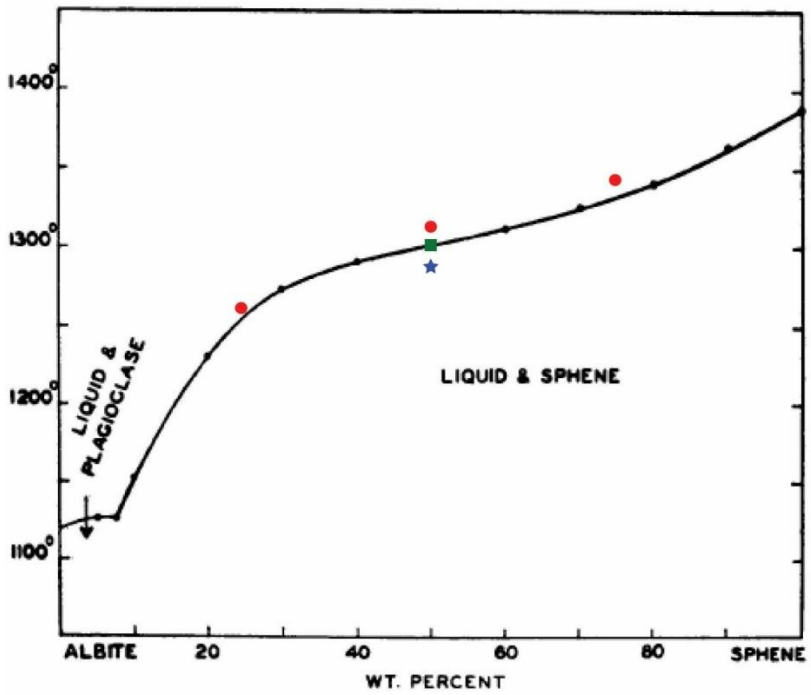

Figure 4. Albite-titanite (sphene) phase diagram mapped by Prince (1943). Superimposed are red dots that represent the experimentally determined liquidi for synthetic starting materials and a green square for natural starting materials at $ttn_{25}ab_{75}$, $ttn_{50}ab_{50}$, and $ttn_{75}ab_{25}$. The blue star represents $\overline{T}$ 1280°C used for the amplitude experiments. Titanite stability covers the majority of temperatures and compositions of this binary system.

The liquidus for $ttn_{50}ab_{50}$ of synthetic and natural starting materials was determined experimentally at 1312°C, 12°C higher than reported by Prince (1943) (Fig 4.). $Ttn_{75}ab_{25}$ and $ttn_{25}ab_{75}$ compositions were tested and both were about 12°C higher than the published liquidus temperatures (Fig. 4). Prince (1943) used similar starting materials, but fused the oxides into glass multiple times, powdering between each fusion to ensure homogenization. Most of his run times for liquidus experiments were short, typically only 30 minutes. With using such homogenized glasses, spontaneous nucleation (homogeneous nucleation), which is slower than nucleation onto pre-existing crystals (heterogeneous nucleation) (Kirkpatrick, 1977) is likely the primary formation mechanism of titanite. Sluggish nucleation combined with some degree of undercooling and short run times could have suppressed Prince's liquidus. However, differences in liquidus temperatures did not affect the experiments because of the broad titanite stability field and all experiments were performed under 1300°C, the lowest reported liquidus for $ttn_{50}ab_{50}$.

Amplitude experiments

Starting material was synthesized mixed from pure oxide and carbonate powders according to the following reaction:

$$7\ SiO_2 + Na_2CO_3 + Al_2O_3 + TiO_2 + CaCO_3 =$$

$$2\ NaAlSi_3O_8\ (albite) + CaTiSiO_5\ (titanite) + 2\ CO_2 \qquad (1)$$

Powder 0.05 μm γ-alumina was used for Al_2O_3, nano-powder anatase for TiO_2, and < 10 μm species of all other oxides and carbonates. $Ttn_{50}ab_{50}$ was mixed by grinding powders in a tungsten carbide ball mill for 5 minutes. The powder was left unfused and unfired to expedite nucleation of titanite crystals at existing oxide crystallographic sites (i.e., Ti and Ca).

Period experiments

Pegmatitic, clear-green titanite from the Delicias Pegmatite Mine, Ensenada, Baja California, Mexico and albite from the Morefield Mine, Virginia (Amelia Albite; Appendix 1) were crushed in a Shatterbox ceramic ring and puck mill for 10 minutes. Powders were mixed to $ttn_{44}ab_{56}$ and fused into glass 80°C above the experimentally determined system liquidus (1300±1°C) for two hours. 10 % titanite was left out in order to add titanite fragments (referred to as 'seeds') to the glass later. After the $ttn_{44}ab_{56}$ glass was re-powdered, 10 % seeds were mixed in by mortar and pestle, bringing the composition to $ttn_{50}ab_{50}$. Titanite seeds are the same composition as titanite in the glass and sieved to < 54 µm length through a cloth mesh in order to control the initial maximum size. Seeds measured from two images contain 1542 crystals and have a median eigenlength (square root of the area) of 0.0042 mm (Fig. 5).

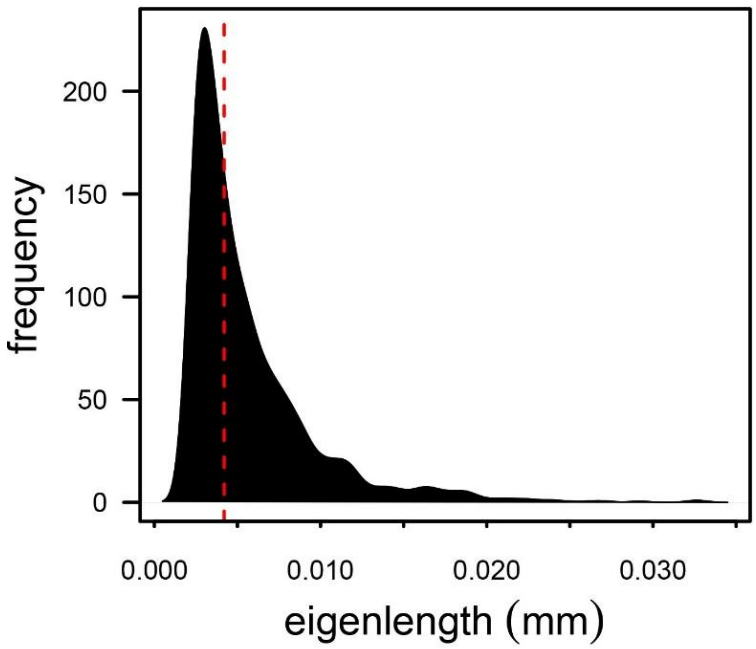

Figure 5. Titanite seed eigenlengths (square root of the area) added to fused ttn-ab glass to comprise 10% of the starting material and an overall composition of $ttn_{50}ab_{50}$. The median value for seeds is marked by the red dashed line at 0.0042 and the characteristic size (S_N) is 7 x 10^{-4} mm (Table 2).

Experimental procedure

The starting material was mixed with distilled water and glue binder solution, which was then dried in a hemispherical Teflon cup onto 0.13 mm Pt wire loops ~ 4 mm in diameter, referred to as charges hereafter. Charges were then hung from two Pt hooks, 1 cm away from a type-S Pt/$PtRh_{10}$ thermocouple calibrated against the melting point of Au (1064°C). Experiments were performed in the hotspot of a Deltech 1-atm, gas mixing vertical tube furnace. Charges were exposed to air where Fe oxidation or Fe loss to Pt were assumed negligible due to the scarcity of Fe in starting materials and its assumed unimportance to titanite growth in the pure $ttn_{50}ab_{50}$ system. Charges were quenched in water by electrically fusing the suspension wires. Quench crystallization is typically displayed by acicular crystals and skeletal crystal formation (e.g. Wyllie et al., 1962) and observations of this phenomenon in charges were rare. Therefore, crystal growth during quenching is assumed negligible.

Temperature cycling was controlled via a programmable Eurotherm 3504 controller and temperatures were logged every 5 seconds. Cycles were programmed as ramp and dwell segments but due to thermal inertia of the system, the resultant cycles were pseudo-sinusoidal (Fig. 6). All cycled experiments were ended with a 30 minute hold at the $\overline{T}$ to stabilize effects of down or up-T swings (Mills and Glazner, 2013). An exception to this procedure was made to look at two experiments quenched at the high and low-T portion of the cycle in order to capture the effects of the end-member T's. These experiments were carried out at a $\overline{T}$ of 1275°C, amplitude of 15°C, and period of 48 mins for 4 cycles (same conditions as NAT-7; Table 2).

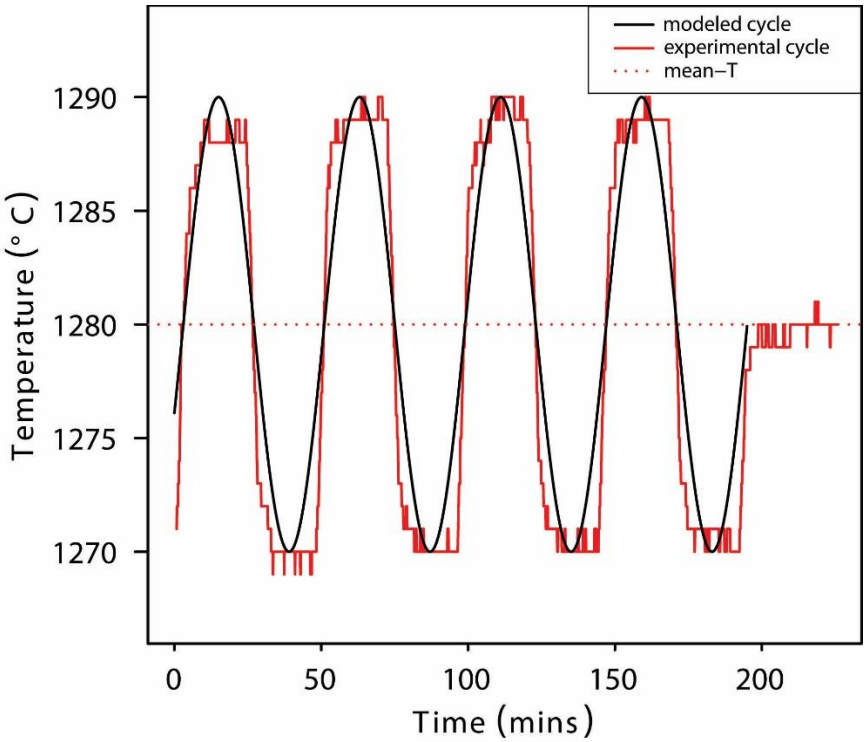

Figure 6. T-t path of a typical observed experimental cycle shown in red. The programmed cycle is parsed between rate and dwell periods. The modeled experimental cycle is the black line. Mean temperature ($\overline{T}$) is shown red dashed line.

Crystal measurement and analysis

Charges were mounted in epoxy with the vertical axis parallel to the plane of polishing. Mounts were polished to the center of the charge to expose a maximum 2D cross section (Fig. 7a). Samples were then carbon coated and imaged with backscattered electrons (BSE) on a Tescan VEGA 1 scanning electron microscope (SEM) at the University of North Carolina, at 15 kV with a typical beam current of 5 nA. Images were passed through a threshold to make binary maps of crystals + glass (crystal = black, glass = white) (Fig. 7, 8, 9) using imageJ software (http://imagej.nih.gov/ij/). Total area and void space were measured so that vesicles and quench cracks were not a part of the total area measurements (Fig. 7c, 8, 9). Three images were analyzed for each experiment using the same scale for size and texture quantification (Fig 8, 9).

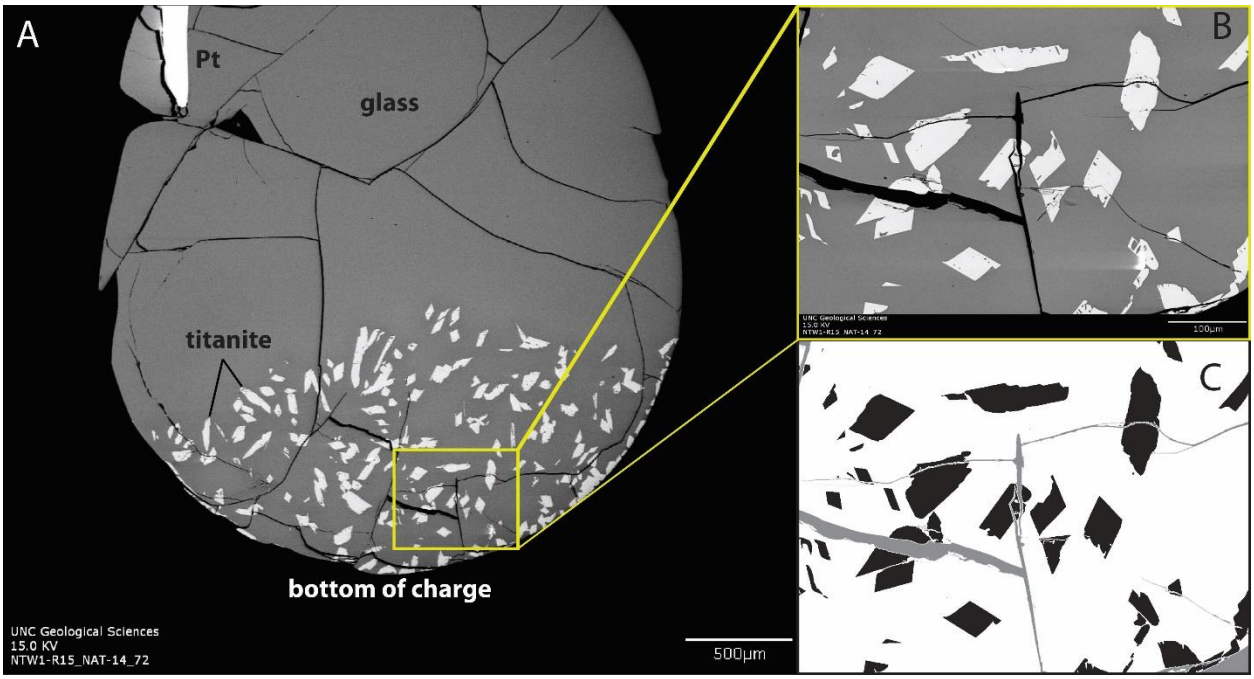

Figure 7. a) Backscattered electron image of a charge (NAT-14). Crystals are concentrated near the bottom of the charge at $\overline{T}$ 1285°C. b) Titanite crystals (white) in an albitic glass (gray). Void spaces such as quench cracks and vesicles are subtracted by processing in imageJ and c) converted to binary images where crystals are measured.

Touching crystals were separated with a watershed tool in imageJ where crystals were too numerous to split manually. The watershed program requires binary images to find the centers of the regions and then uses a dilation function to find where regions first touch, drawing a boundary along that line. This technique works best with rounded regions. Where volumetric number densities exceeded ~1 x 10^6 mm^{-3} especially in short, low-amplitude runs, titanite had a higher degree of rounding. The images were then touched up manually to correct any single crystals that were severed by the watershed function. There is a degree of subjectivity when cutting crystals but this method is sufficient because the number of ambiguous situations is small compared to the number of crystals analyzed (Mills and Glazner, 2013).

Crystal area fraction (Φ) and crystal area number density (N_A) (mm^{-2}), or the number of crystals per unit area, were calculated for each experiment following procedures from Mills and

Glazner (2013) and Blundy and Cashman (2008). These are used to calculate the characteristic length (S_N) for each batch of crystals using:

$$S_N = (\phi/N_A)^{0.5} \text{ (mm)} \quad (2)$$

N_A can be extrapolated to N_V, the number per unit volume, based on intersection probabilities (Underwood, 1970) using:

$$N_V = N_A/S_N = N_A/(\phi/N_A)^{0.5} \text{ (mm}^{-3}\text{)} \quad (3)$$

Crystal batch growth rate (G_{batch}) was determined by dividing S_N by time (Eq. 4) (Hammer and Rutherford, 2002; Blundy and Cashman, 2008; Mills and Glazner, 2013). In period experiments, S_N of titanite seeds was subtracted from each experimental S_N to observe minimum growth rates; this term is zero for unseeded runs.

$$G_{batch} = (S_N - S_N^{seed})/t \text{ (mm/s)} \quad (4)$$

Maximum growth rates were calculated following Mills and Glazner (2013) by using the median eigenlength of the 10 ($^{10}A_{max}^{0.5}$) and 50 ($^{50}A_{max}^{0.5}$) largest crystals for each experimental condition (Eq. 5, 6). Median values were favored over means because they are less sensitive to anomalously large crystals (Mills and Glazner, 2013) and means are highly dependent on the number of crystals measured (Higgins, 2006).

$$^{10}G_{max} = {}^{10}A_{max}^{0.5}/t \text{ (mm/s)} \quad (5)$$

$$^{50}G_{max} = {}^{50}A_{max}^{0.5}/t \text{ (mm/s)} \quad (6)$$

Areas of the largest 50 crystals were extrapolated to volumes by $(A_{max})^{1.5}$ (mm^3). CSDs were measured for period experiments using *CSDcorrections*. CSDs for titanite were calculated using the minor axis of each crystal, which is appropriate for prismatic shapes (Higgins, 2000). A ratio of 1:2:3 was used for the shape of titanite and a roundness of 0.2 based on the simplified unit cell of titanite. This shape was confirmed with *CSDslice* software which measures the best

fit shapes based on intersection probabilities of a 2D surface (Morgan and Jerram, 2006). Modal intersections of width/length are similarly used in CSD corrections to fit 3D shape aspects (Higgins, 2000). Crystals under 5 μm^2 were not evaluated due to the limits of image resolution.

RESULTS

Qualitative crystal textures

Synthetic oxide starting materials yielded small, interconnected networks of titanite in an albite-rich glass (Fig 8). A very short run (15 min) was performed to observe how the oxides produced the two phases before they reached thermal equilibrium. Quartz was seen as a rare, anhedral phase that was larger than already well-established titanite crystals. Experiments longer than 2 hours had no quartz, and titanite morphology became increasingly euhedral with increasing amplitude compared to static conditions (Fig. 8). Nucleation of titanite from the oxides produced large crystal number densities (N_A), and some melt pockets occupied by larger crystals (e.g. Fig. 8, static at 100-h and α 10°C at 100-h).

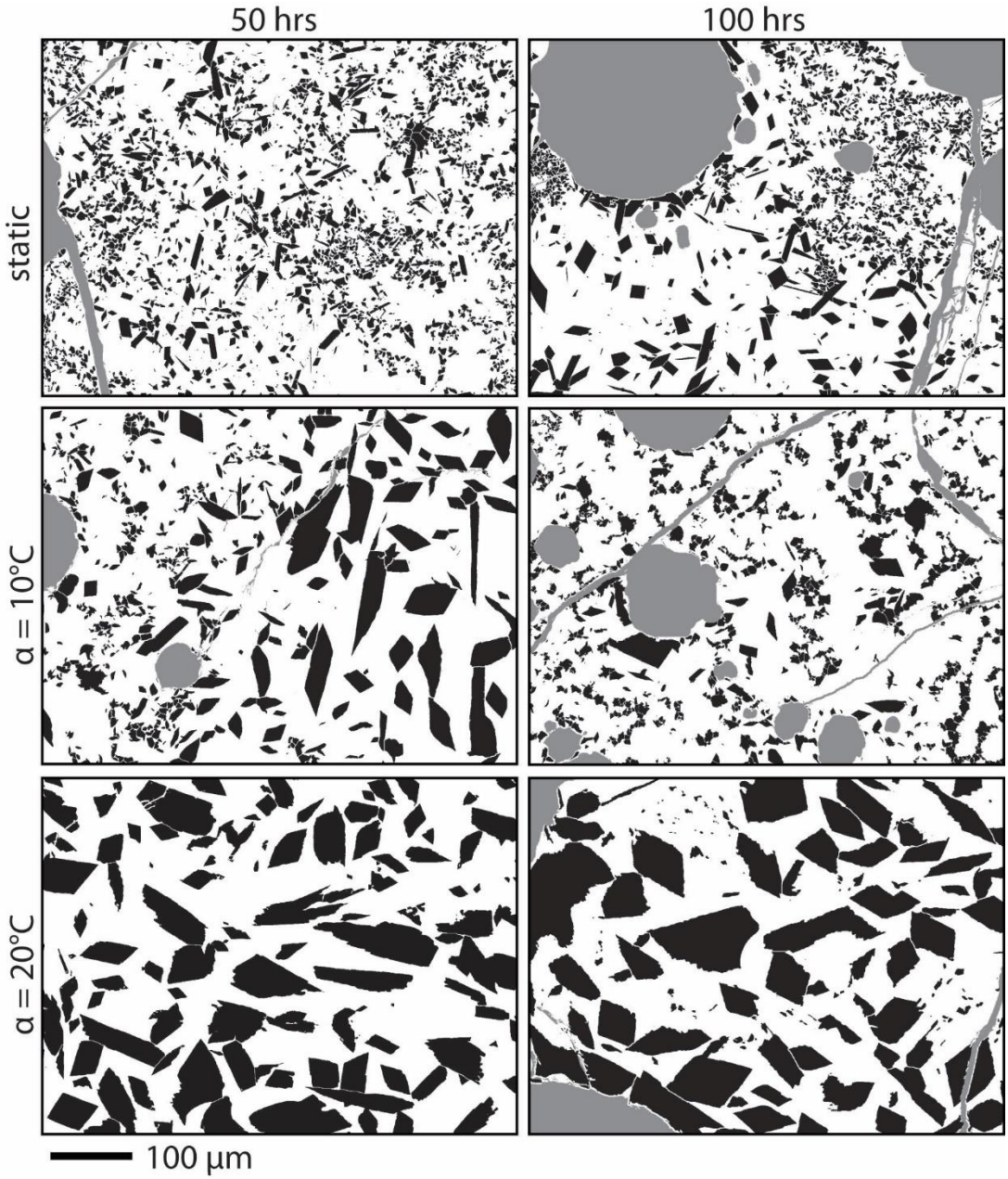

Figure 8. Processed images from α experiments with columns representing 50 and 100-h runs, and rows representing static, α 10 and 20°C. Titanite crystals are black regions in glass (white), gray areas are void spaces that were subtracted from overall area measurements. Titanite is qualitatively larger with time and α

Table 2. Amplitude experiments data

Run	Amplitude α (°C)	Time (h)	N_A (mm^{-2})	ϕ	S_N (mm)	N_V (mm^{-3})	G_{batch} (mm/s)	median 50 A_{max} (mm)	G_{max} (mm/s)
D77	0	2.2	7239	0.26	0.0059	1.22E+06	7.50E-07	0.0177	2.24E-06
D84	0	8.2	9248	0.21	0.0047	1.96E+06	1.60E-07	0.0119	4.02E-07
D46	0	21.6	8554	0.17	0.0045	1.92E+06	5.73E-08	0.0069	8.83E-08
D32	0	47.1	5547	0.20	0.0060	9.20E+05	3.56E-08	0.0166	9.80E-08
D67	0	116.4	5770	0.22	0.0062	9.35E+05	1.47E-08	0.0187	4.46E-08
D79c	5	2.2	7871	0.20	0.0050	1.58E+06	6.30E-07	0.0138	1.74E-06
D66c	5	8.5	6265	0.19	0.0055	1.13E+06	1.81E-07	0.0222	7.25E-07
D82c	5	20	6168	0.24	0.0063	9.79E+05	8.75E-08	0.0142	1.98E-07
D75c	5	50.3	3280	0.18	0.0075	4.40E+05	4.12E-08	0.0238	1.31E-07
D81c	5	99.9	3024	0.22	0.0085	3.57E+05	2.36E-08	0.0185	5.15E-08
D61c	10	1.9	6532	0.21	0.0057	1.16E+06	8.26E-07	0.0163	2.38E-06
D60c	10	10.5	7062	0.19	0.0053	1.34E+06	1.39E-07	0.0140	3.71E-07
D59c	10	21.9	2778	0.20	0.0086	3.24E+05	1.09E-07	0.0257	3.26E-07
D70c	10	50.7	1618	0.29	0.0134	1.21E+05	7.35E-08	0.0305	1.67E-07
D58c	10	89.6	3519	0.23	0.0080	4.38E+05	2.49E-08	0.0162	5.01E-08
D76c	10	121.7	2039	0.22	0.0104	1.95E+05	2.38E-08	0.0329	7.52E-08
D80c	15	2.1	5765	0.17	0.0055	1.05E+06	7.26E-07	0.0152	2.02E-06
D65c	15	8.3	5861	0.20	0.0059	9.94E+05	1.97E-07	0.0166	5.56E-07
D68c	15	24.5	3781	0.27	0.0085	4.46E+05	9.62E-08	0.0202	2.29E-07
D62c	15	47.5	2783	0.24	0.0093	3.00E+05	5.42E-08	0.0349	2.04E-07
D41c	15	101.1	2077	0.29	0.0119	1.75E+05	3.27E-08	0.0319	8.76E-08
D49c	20	2.3	11704	0.21	0.0043	2.73E+06	5.17E-07	0.0082	9.90E-07
D48c	20	8.1	8429	0.18	0.0046	1.85E+06	1.56E-07	0.0093	3.19E-07
D50c	20	20.2	6235	0.24	0.0062	1.01E+06	8.49E-08	0.0145	2.00E-07
D69c	20	69.7	3252	0.28	0.0093	3.51E+05	3.69E-08	0.0482	1.92E-07
D83c	20	99.4	743	0.32	0.0206	3.60E+04	5.77E-08	0.0387	1.08E-07

Period experiments (natural starting materials) contained subhedral to euhedral titanite in an albitic glass. There are more vesicles in static runs than in cycled runs (Fig. 9). Titanite crystals, especially at the high $\overline{T}$ of 1285°C, only occupied the bottom of the charge (Fig. 7a) and in some cases had skeletal crystals in the transition from the top of the charge (crystal poor) to the bottom (crystal rich). Crystals in cycled runs are larger and more euhedral than in static runs (Fig. 9).

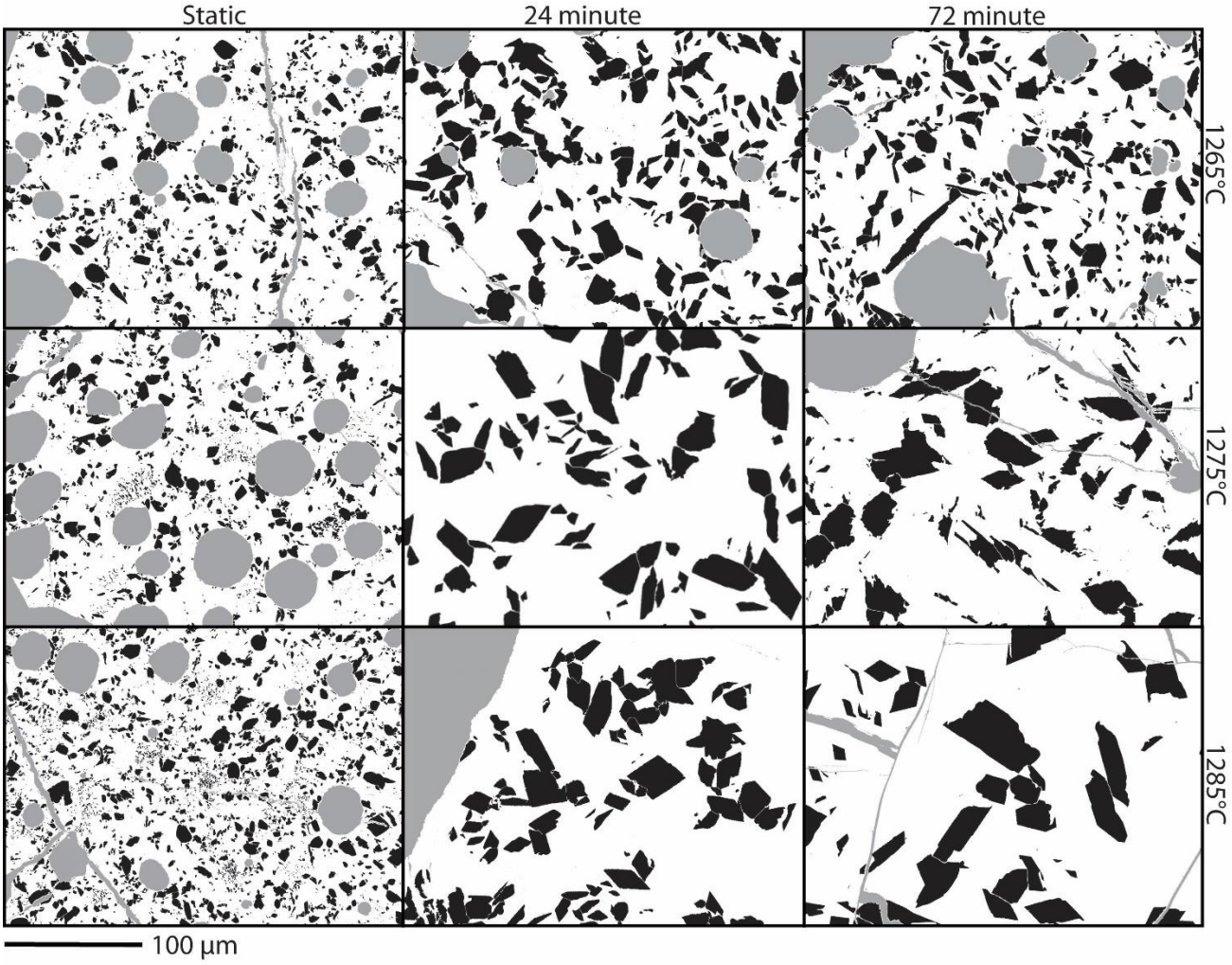

Figure 9. Binary images from τ experiments with columns of static, shortest and longest period tested. Rows separate the three mean temperatures. An amplitude of 15°C and duration of 50-h was used for all τ experiments. Cycled runs contain larger, more euhedral crystals than static conditions.

Table 3. Period experiments data

Run	Period (min)	Cycle (#)	$\overline{T}$ (°C)	N_A (mm^{-2})	S_N (mm)	N_V (mm^{-3})	G_{batch} (mm/s)	Median 10 $A^{0.5}{}_{max}$ (mm)	Median 50 $A^{0.5}{}_{max}$ (mm)	$^{10}G_{max}$ (mm/s)	$^{50}G_{max}$ (mm/s)
NAT-23	0	0	1265	1829	0.0095	1.93E+05	1.47E-08	0.0425	0.0301	7.36E-08	6.01E-08
NAT-15	24	125	1265	555	0.0194	2.86E+04	6.97E-08	0.0523	0.0357	1.75E-07	1.47E-07
NAT-16	48	63	1265	911	0.0155	5.86E+04	4.84E-08	0.0469	0.0388	1.49E-07	1.28E-07
NAT-17	72	42	1265	879	0.0161	5.47E+04	5.13E-08	0.0551	0.0378	1.8E-07	1.18E-07
NAT-22	0	0	1275	2343	0.0088	2.66E+05	1.09E-08	0.0562	0.0374	9.41E-08	6.46E-08
NAT-5	24	125	1275	416	0.0215	1.94E+04	8.13E-08	0.0523	0.0358	1.49E-07	9.61E-08
NAT-6	36	83	1275	558	0.0195	2.87E+04	7.01E-08	0.0373	0.0319	1.18E-07	1.13E-07
NAT-7	48	63	1275	330	0.0237	1.39E+04	9.35E-08	0.0719	0.0547	1.64E-07	1.08E-07
NAT-8	60	50	1275	348	0.0235	1.48E+04	9.27E-08	0.0670	0.0478	1.7E-07	1.05E-07
NAT-9	72	42	1275	864	0.0146	5.91E+04	4.33E-08	0.0686	0.0465	1.49E-07	9.62E-08
NAT-21	0	0	1285	3341	0.0079	4.21E+05	6.01E-09	0.0614	0.0428	6.52E-08	7.49E-08
NAT-20	24	125	1285	266	0.0281	9.47E+03	1.18E-07	0.0625	0.0410	2.58E-07	2.02E-07
NAT-11	36	83	1285	276	0.0299	9.23E+03	1.28E-07	0.0388	0.0293	2.3E-07	1.63E-07
NAT-12	48	63	1285	462	0.0219	2.11E+04	8.37E-08	0.0570	0.0449	2.39E-07	1.56E-07
NAT-13	60	50	1285	175	0.0329	5.32E+03	1.45E-07	0.0524	0.0415	1.99E-07	1.35E-07
NAT-14	72	42	1285	119	0.0368	3.24E+03	1.66E-07	0.0580	0.0397	2.06E-07	1.25E-07

Crystal number densities

Decrease of N_V with time in amplitude experiments is variable under 50-h, attaining a more stable trend over longer durations (Fig. 10a). Cycled amplitude experiments exhibited lower N_V than static experiments, which show the smallest N_V change over time (Fig. 10a). The lowest N_V are in the two longest-period experiments (τ 60, 72 min) at $\overline{T}$ 1285°C (Fig. 11a) (Table 2). N_V values in cycled period experiments are about one order of magnitude lower than in static runs (Fig. 11a), but there is not a clear trend with period. The presence of titanite seeds in the period experiments has a strong effect on N_V, as shown by static experiments, where N_V is 2 orders of magnitude less in seeded experiments than in experiments run on synthetic starting materials.

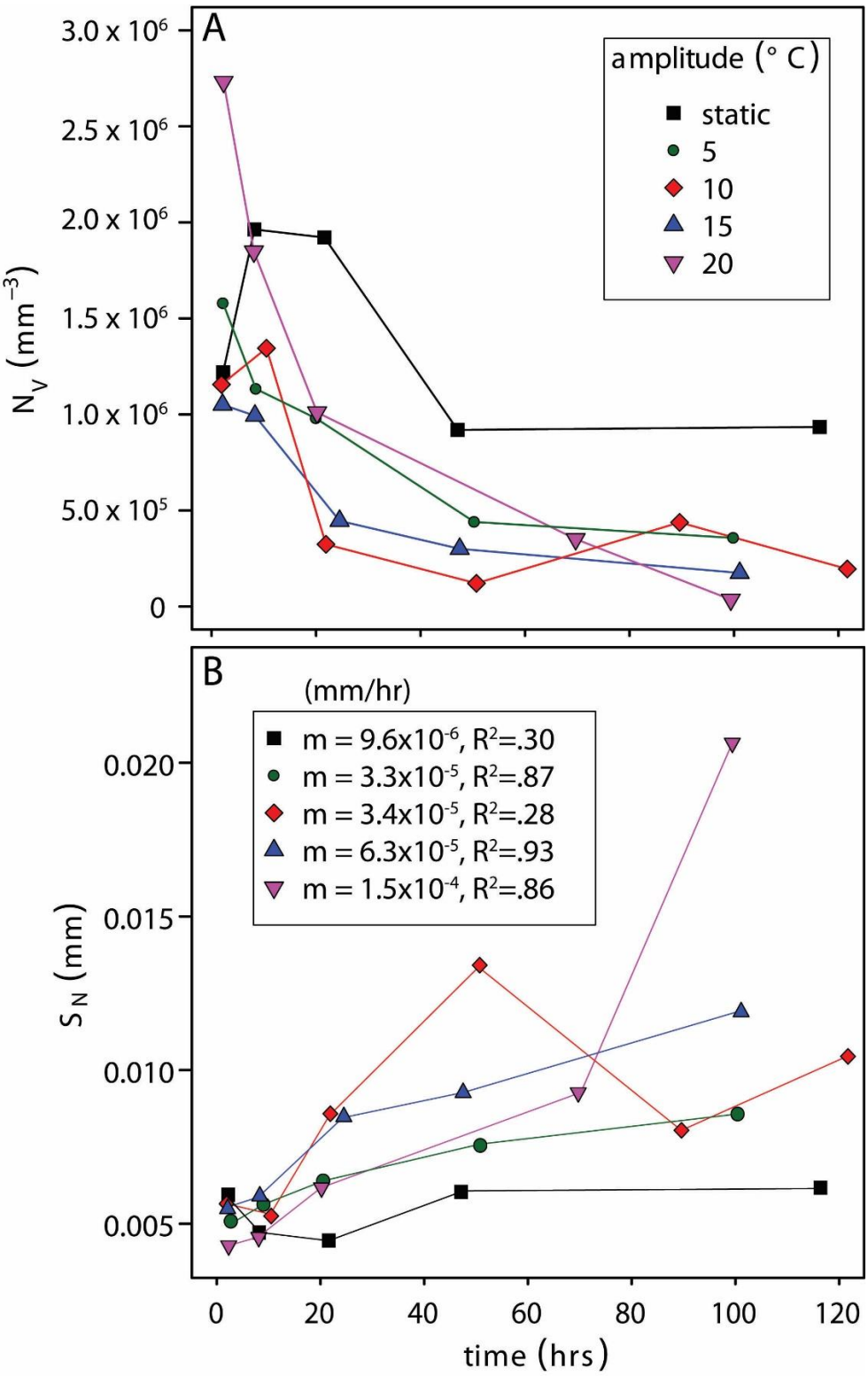

Figure 10. a) Crystal number density (N_V mm^{-3}) versus time for amplitude experiments. b) Characteristic size (S_N mm) (eq. 2) versus time where m = slope of a best fit trend line (mm/s).

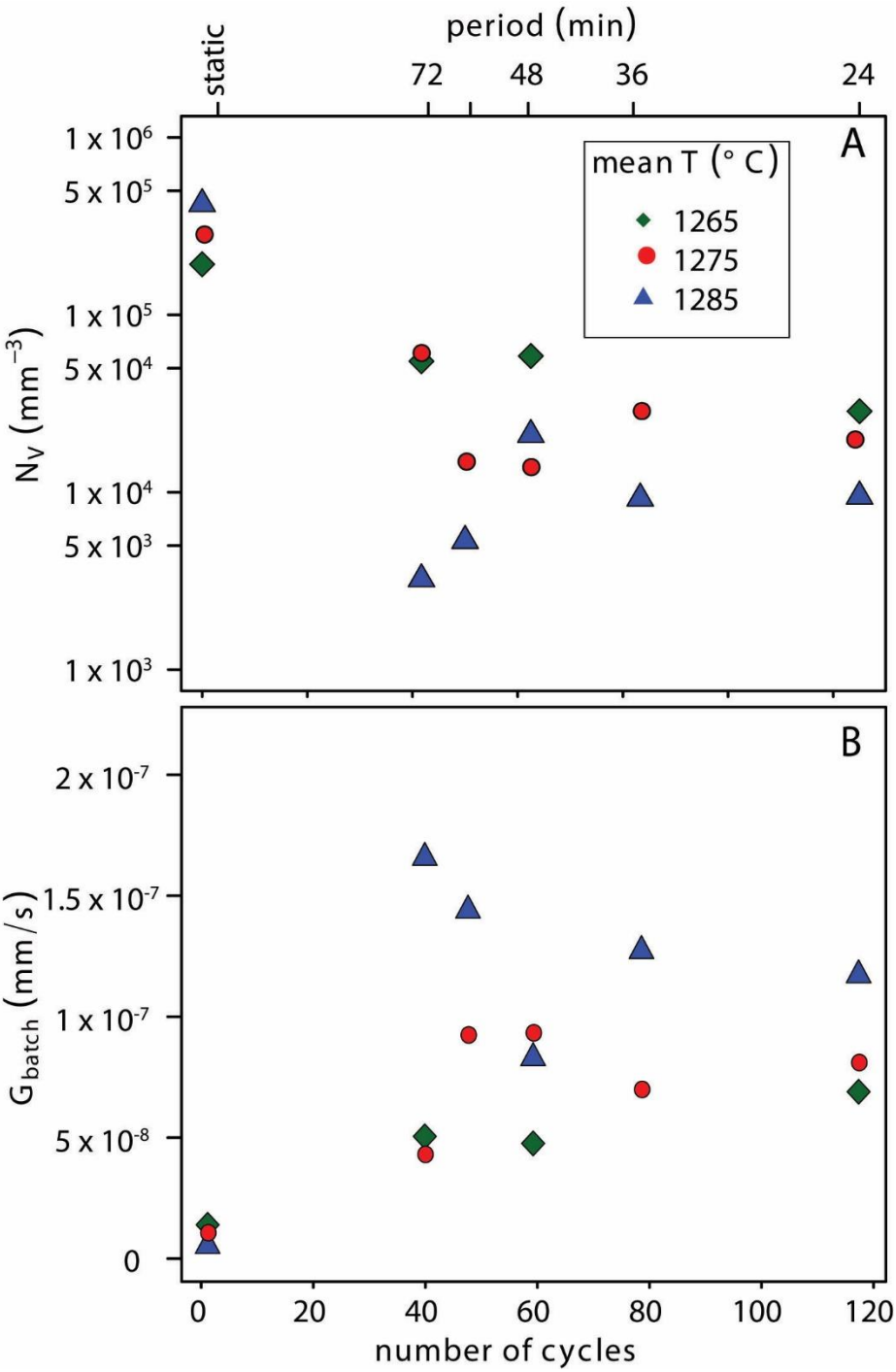

Figure 11. a) Log plot of the crystal number density (N_V mm^{-3}) versus cycles related by period (cycles = $1/\tau$) for three mean temperatures. Black squares represent seed N_V for reference. b) G_{batch} (mm/s) versus cycles for three mean temperatures.

Titanite growth rates

For each amplitude investigated, G_{batch} growth rates decrease with time (Fig. 12). Growth rates calculated from S_N are on the order of 10^{-6} mm/s (Fig. 10b) which are greater than the amplitude G_{batch} estimates of 10^{-7} mm/s (Fig. 12). Amplitude experiments G_{batch} rates are 4 times greater for 2-h durations (Fig. 12) but G_{batch} rates for longer durations show little increase with amplitude.

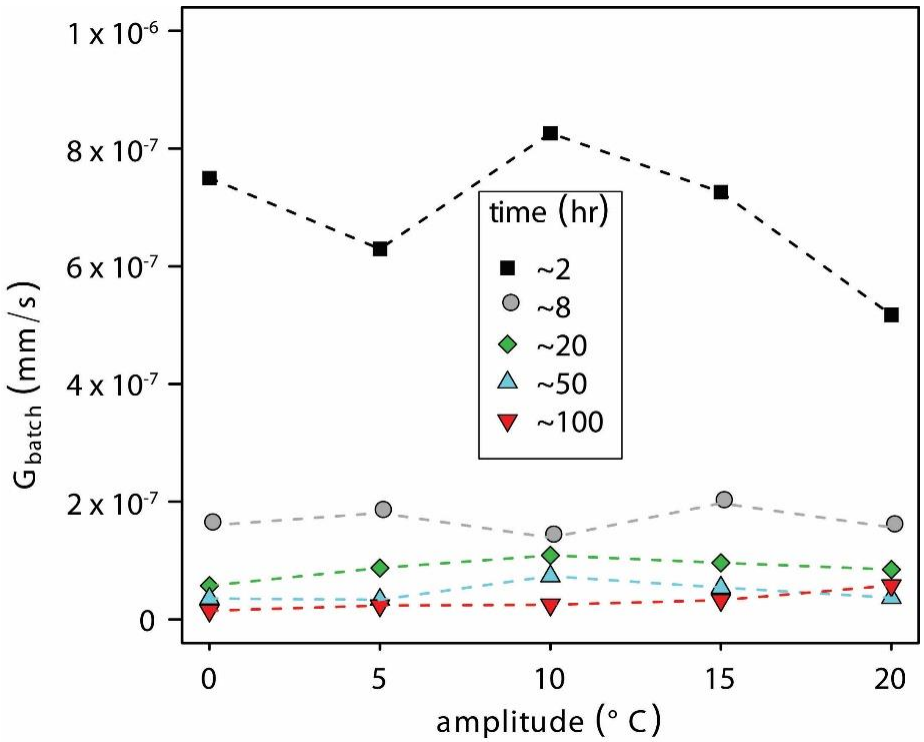

Figure 12. G_{batch} rates versus amplitude, separated by approximate experiment durations (hours). Growth rates decrease by a factor of four from 2 to 8 hours.

G_{batch} rates for period experiments show $\overline{T}$ 1285°C rates that are larger than the overlapping rates of $\overline{T}$ 1265°C and 1275°C (Fig. 11b). $^{50}G_{max}$ rates increase with the number of cycles, or the inverse of the period, but do not increase with $\overline{T}$ because $\overline{T}$ 1265°C rates are greater than 1275°C rates (Fig. 13b).

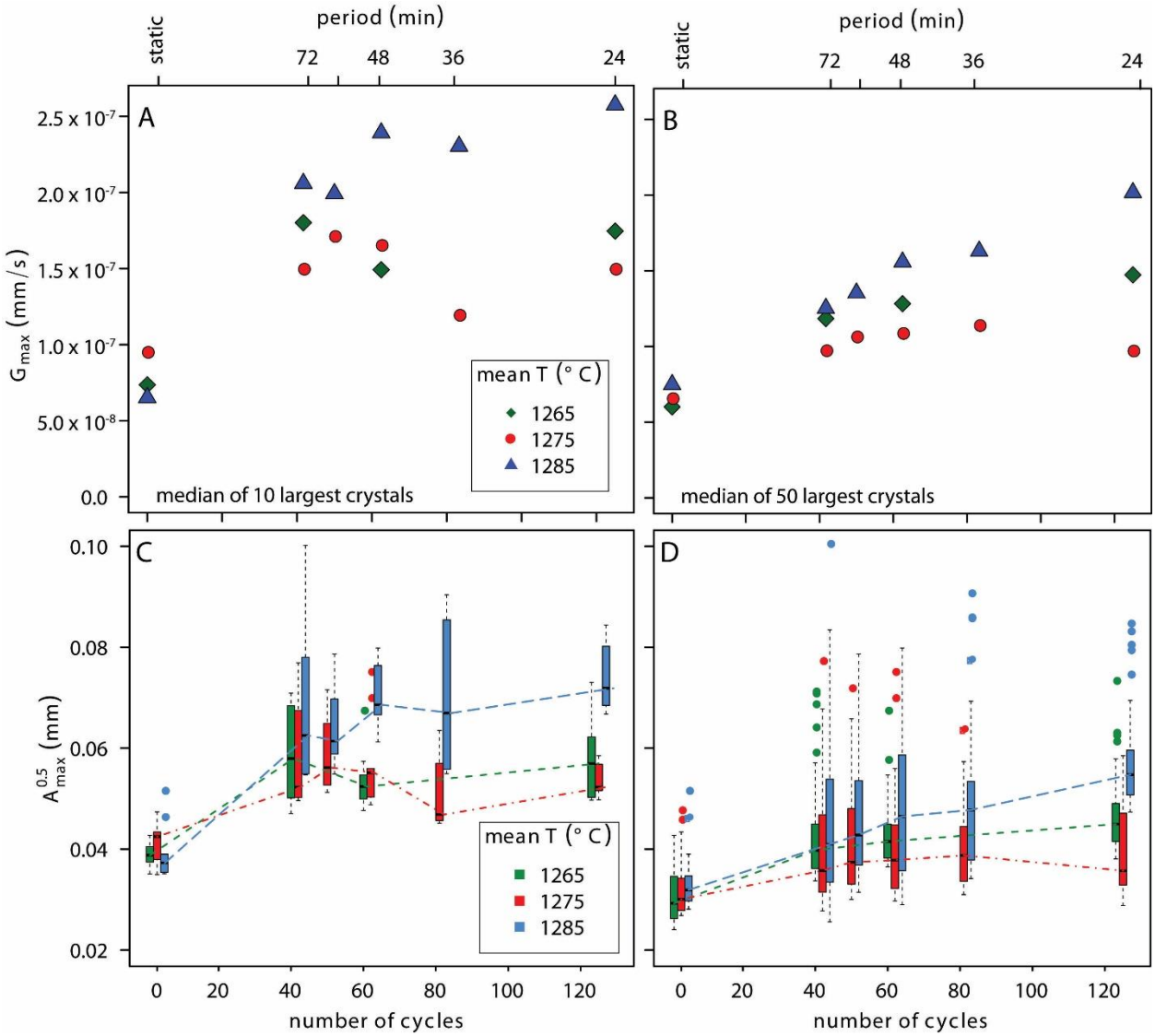

Figure 13. a) Growth rates of the largest 10 crystals ($^{10}G_{max}$) and b) 50 crystals ($^{50}G_{max}$) for $\overline{T}$'s plotted against both number of cycles and period. Boxplots show the median distributions for the c) largest 10 ($^{10}A^{0.5}_{max}$) and d) 50 ($^{50}A^{0.5}_{max}$) eigenlengths. Outlier points fall outside the upper quartile.

Volume estimates and CSDs in τ experiments

Volumes of the 50 largest crystals increased for all $\overline{T}$ and periods compared to static volumes by mass transfer from smaller crystals to larger ones with fixed overall crystal proportions (Φ) (Fig. 14). Volumes for the 10 largest crystals increased by a factor of 4 above static sizes (Fig. 14). Volumes do not trend with period, but $\overline{T}$ 1285°C volumes reach larger sizes

(> 5 x 10^{-4} mm^3) that are greater than the largest crystals measured for $\overline{T}$ 1265°C and 1275°C (Fig 14a, b, c).

CSDs for the three $\overline{T}$'s are concave up. (Fig. 14a, b, c). CSDs for $\overline{T}$ 1285°C for periods 36, 60, and 72 min have a break in slope in population sizes near ~40 μm (Fig. 14c). CSDs for each $\overline{T}$ are mostly similar and do not trend regularly with period. However, cycled CSDs systematically have lower slopes than static CSDs. CSDs for the two experiments quenched at the high and low-T ends of the cycle (Fig. 14d) show that the low-T quench run is elevated above the steeper high-T quench run.

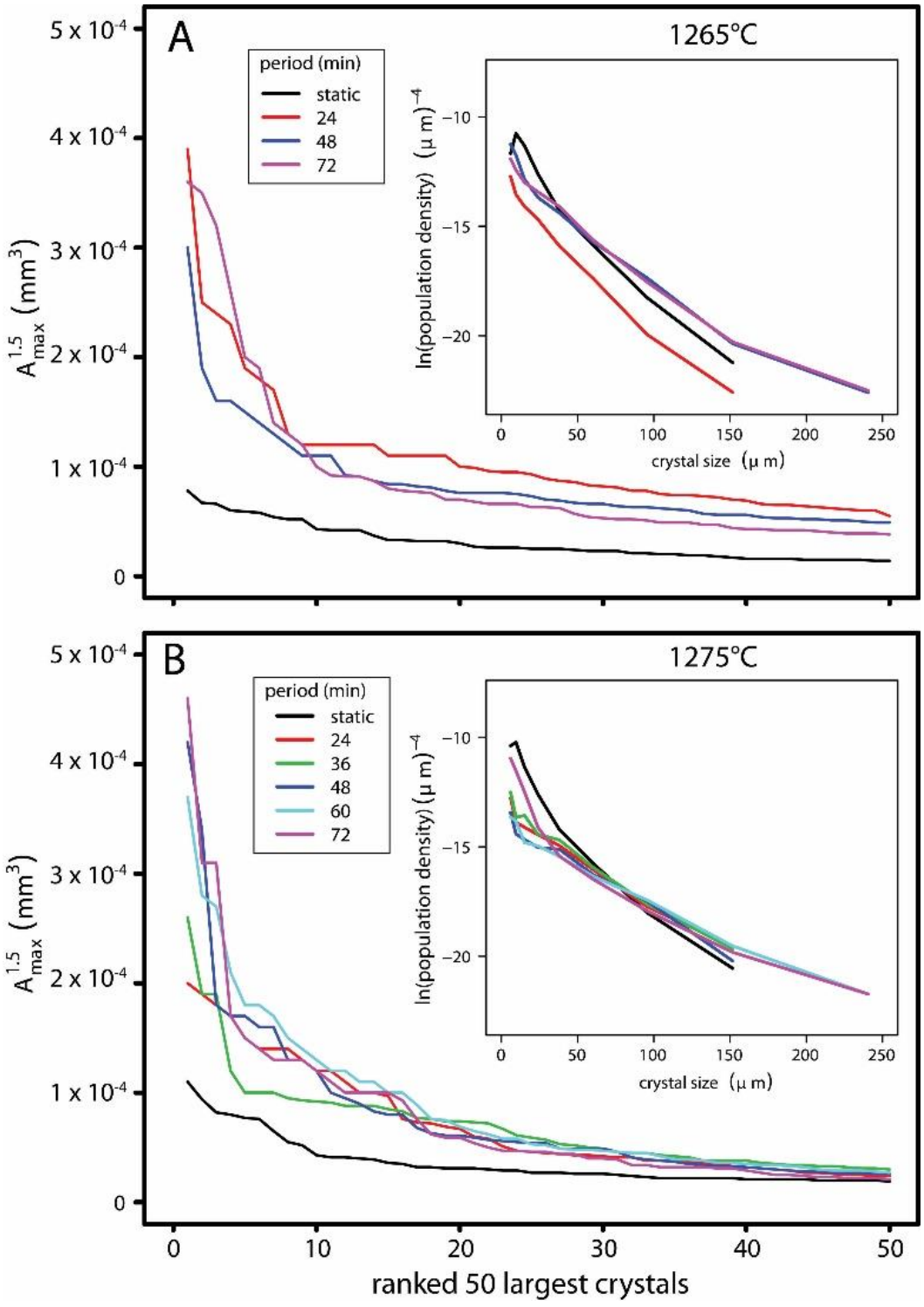

Figure 14. Volume estimates of A_{max} for $\overline{T}$'s a) 1265°C and b) 1275°C, and c) 1285°C with inset CSDs for the 50 largest crystals. Seeds are dashed lines. CSDs truncate at low crystal sizes because sizes smaller than 5 μm^2 were not measured. With the total crystal volume constant in period experiments, mass transfer to the largest 10 crystals is from smaller crystal sizes.

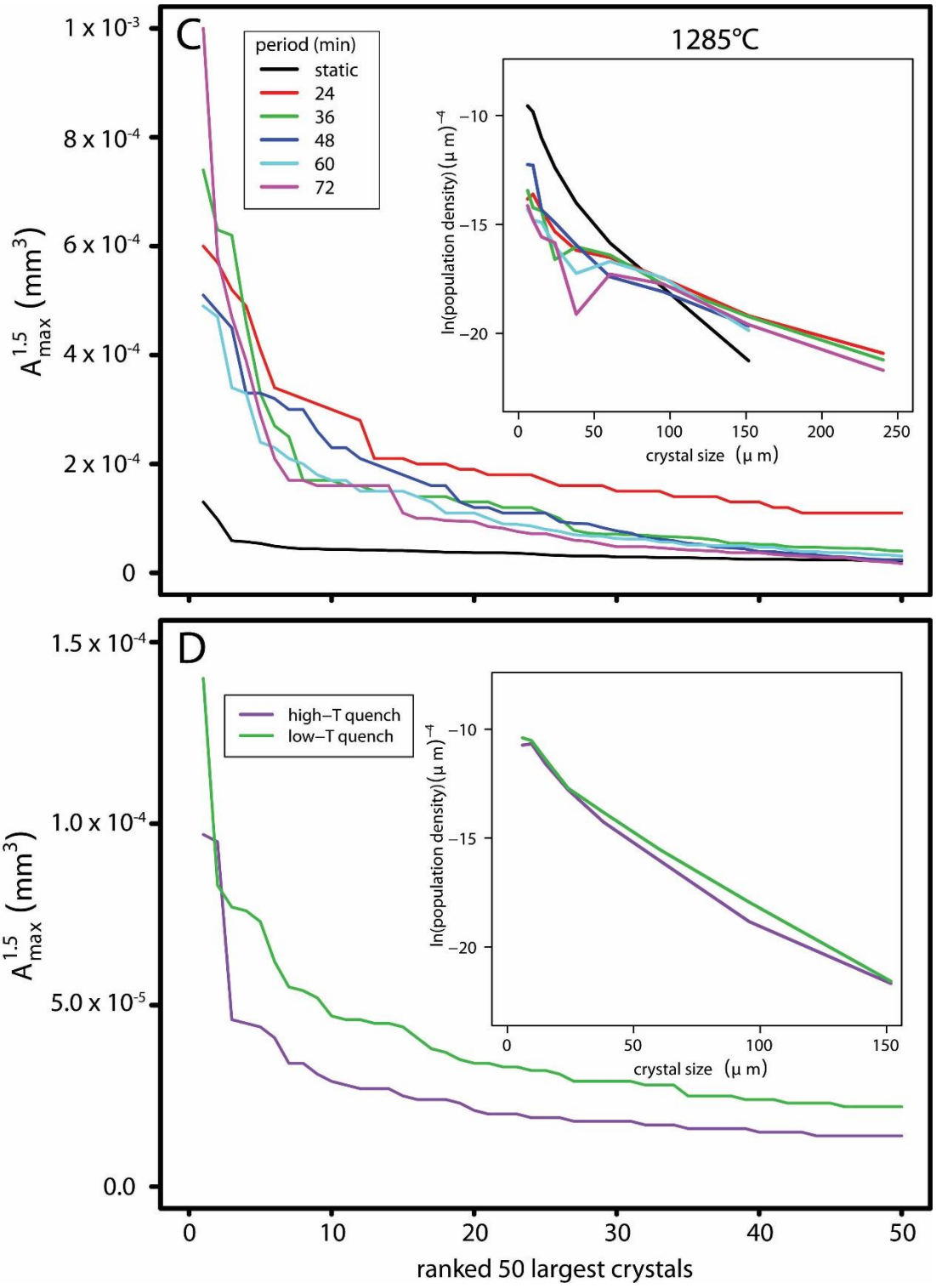

Figure. 14 continued Volume estimates of A_{max} for $\overline{T}$'s c) 1285°C with inset CSDs for the 50 largest crystals. d) Volumes and CSDs of two experiments quenched at the high and low-T portion of the cycle ($\overline{T}$ 1275°C, α 15°C for 4 cycles).

DISCUSSION

Crystal destruction

Static T

In amplitude experiments, the overall decrease in N_V with time is consistent with little or no crystal nucleation (Zieg and Lofgren, 2006; Mills et al., 2011; Mills and Glazner, 2013). Mills and Glazner (2013) used a basaltic starting material in which crystals fully equilibrated with the liquid phase in the first 20-h of experimentation. Rapid decrease in N_V in the first hour for their experiments was likely accelerated by high concentrations of crystal dislocations from crushing the sample close to its comminution limit (Glazner and Mills, 2012). However, our starting material was mixed from synthetic oxides with no existing titanite crystals, so it is not likely to share this problem. It is more likely that titanite and liquid are concurrently forming from the oxides with rapid increase in temperature. Titanite forming from oxides heterogeneously nucleates on pre-existing sites while observed melt pockets could be left by dissolving metastable quartz grains. SiO_2 dissolution is a rate-limiting diffusive component (e.g. Watson, 1982) and could be the last metastable oxide to dissolve before equilibrium temperatures are reached. This would leave no nucleation sites for titanite to grow initially where quartz is dissolving, creating high-silica melt pockets. Later, titanite could nucleate in these melt pockets where they have more space to grow larger than the areas of densely packed crystals (Fig. 8, static at 100-h and α 10°C at 100-h).

Amplitude static experiments in this study (Fig. 10a) decreased in N_V at a rate of -8.2 x 10^3 $mm^{-3}h^{-1}$ over 20-h. Ostwald ripening caused by the size-dependent solubility of crystals

likely aids in the destruction of crystals past 20-h (Cabane et al., 2005; Mills and Glazner, 2013). Composition and melt viscosity strongly affect Ostwald ripening, and the rate of crystal destruction is controlled by growth/dissolution kinetics at solid-liquid interfaces (Cabane et al. 2005). Cabane et al. (2005) found a rate decrease for N_V of -2.3 x 10^3 $mm^{-3}h^{-1}$ for plagioclase in an andesite at 1-atm. Mills and Glazner (2013) found a rate for plagioclase in basalt of -7.6 x 10^3 $mm^{-3}h^{-1}$, suggesting that the increased rate in the basalt experiments was related to lower viscosity of the melt. N_V destruction rates for titanite are not directly comparable because they ran at hotter temperatures than the andesite and basalt (130 and 30°C respectively). However, because the magnitudes of the rate decrease for N_V are similar, the controls for static coarsening are likely similar.

Amplitude and period

N_V for amplitude experiments decreases at a rate of about -8.8 x 10^4 $mm^{-3}s^{-1}$ in the first 20-h and significantly flattens with longer durations (Fig. 10a). Sluggish crystal destruction over 50-h is likely due to the smallest crystals attaining sizes large enough to survive complete dissolution on the up-T portion of a cycle. N_V approaches a new textural equilibrium state where the rate of crystal destruction approaches zero. Cycling does not drive N_V to zero for a given amplitude, but reaches a N_V limit related to amplitude. Thus, consistent N_V decrease in thermal oscillating environments is likely controlled by the preferential dissolution of small crystals by the up-T swing of the cycle and sustained by size-dependent crystallization on the down-T swing (Eberl et al., 2002; Simakin and Bindeman, 2008; Mills and Glazner, 2013). Amplitude has the most control on thermal cycling, but other variables that may play a role in more complex systems are the viscosity of the melt, and the initial nucleation density.

Period does not affect N_V significantly (Fig. 11a). N_V for period experiments slightly decreases with decreasing period for $\overline{T}$'s 1265°C and 1275°C by a maximum of 30 mm^{-3} but is not a significant amount when compared to the number of crystals measured (Table 2). There is no control on N_V by the degree of undercooling, or the distance of the $\overline{T}$ from the liquidus. However, it should be noted that N_V for period experiments is largely restricted by the initial titanite seeds added to the starting material.

Temperature cycling effects on growth rate

Comparing growth rates

G_{batch} rates for amplitude experiments (Fig. 12) decrease with time and are dependent on N_A because the proportion of crystals throughout the experiments is held constant (mean Φ = 0.23, σ_1 = 0.06) (Eq. 2, 3). Amplitude G_{batch} rates at ~2-h are greater than longer-duration experiments by a factor of 4 (Fig. 12) likely due to high nucleation rates and formation from the oxides. Nucleation, although often viewed separately from growth, requires an interval of growth to be observed (Kirkpatrick, 1977; Higgins, 2006). The typical observation for nucleation is that it occurs over a short period of time at a high degree of supersaturation (Lasaga, 1998; Eberl et al., 2002). G_{batch} rates better represent nucleation rates because of the dependence on the population density and are unrepresentative of maximum growth rates. Linear growth rates calculated from the characteristic size (S_N) (Fig. 10b) are better estimates of growth associated with amplitude.

Growth rates associated with varied periods are best represented by G_{max} estimates because they are assessed for two median ranges of 10 and 50 crystals and directly characterize growth in the largest grain sizes. G_{batch} for period experiments is a reflection of N_V because Φ is relatively constant (0.2) and time is constant (50-h). For example, G_{batch} values for $\overline{T}$ 1285°C,

when the period is 60 or 72 min are about 1 x 10^{-7} mm/s greater that the others due to low amounts of crystals measured (Table 2).

Growth effects of amplitude

Growth rates estimated from S_N (Fig. 10b) values increase by a factor of 10 from 5°C to 20°C amplitude and this increase is the primary control of thermal cycling effects on crystal coarsening (Mills and Glazner, 2013). Crystal coarsening is dependent on the amount of crystal solute available from dissolution during the up-T cycle and crystallization on the down-T cycle (Mills and Glazner, 2013). Crystals are coarsened by the integrated effects of size dependent growth (Eberl et al. 2002), and growth dispersion (Girolami and Rousseau, 1985). Growth dispersion, or the variable growth of similar-sized crystals, effectively displaces crystals to oversized bins. These two phenomena are difficult to separate, but act together to grow large crystals faster than smaller ones (Mills and Glazner, 2013).

The distribution of the eigenlength of the largest 50 crystals ($^{50}A_{max}^{0.5}$) increase overall with amplitude through time (Fig. 15), but decrease from 50 to 100-h. Size limitations at long durations probably relates to a restriction of N_V as the system becomes texturally mature. If no more small crystals are easily dissolved by temperature oscillations, growth of large crystal will slow, limited by sluggish self-dissolution.

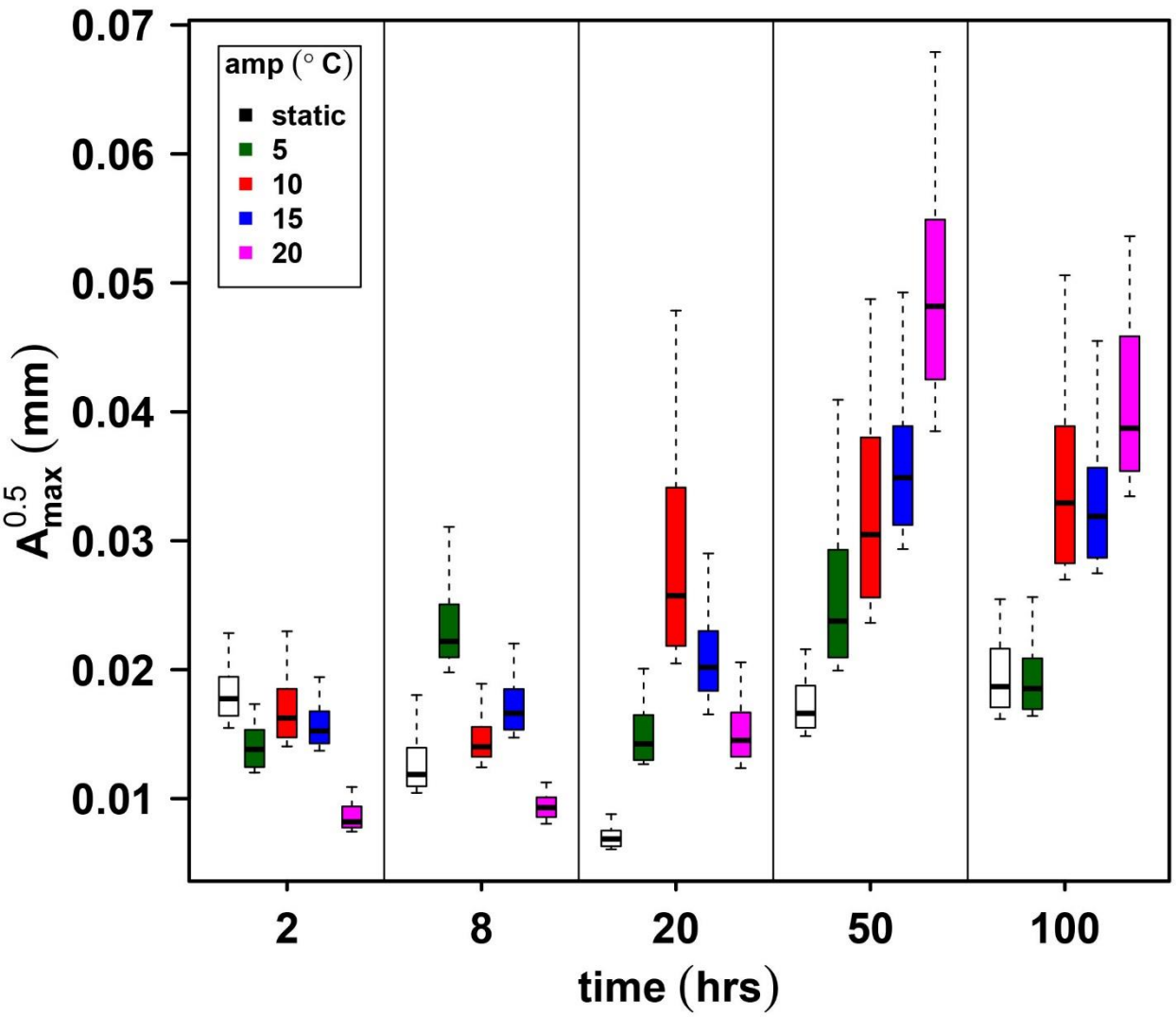

Figure 15. Boxplots of the largest 50 crystal eigenlengths ($^{50}A_{max}^{0.5}$) for all amplitudes. Boxplots are grouped to the durations of 2, 8, 20, 50 and 100-h.

Growth effects of period

$^{50}G_{max}$ for period experiments increase with decreasing period but do not increase consistently with $\overline{T}$ (Fig. 13b). $\overline{T}$ 1265°C has greater $^{50}G_{max}$ rates than $\overline{T}$ 1275°C, but could be explained by $^{50}A_{max}^{0.5}$ (Fig. 13d). The maximum median distribution (Fig. 13d) of $\overline{T}$ 1275°C has a 15 µm larger range than $\overline{T}$ 1265°C. Thus, even though the median values are similar, the distribution of sizes for $\overline{T}$ 1265°C has a narrower dispersion of growth. $^{10}G_{max}$ rates do not show a regular increase with the number of cycles, but elevated $^{10}G_{max}$ for $\overline{T}$ 1285°C (Fig. 13a)

suggests that if thermal cycling passes within 10°C of the liquidus, crystals will be significantly coarsened. However, it is assumed that overstepping the liquidus will cause dissolution and subsequent destruction of all crystals present (Mills and Glazner, 2013).

Elevated G_{batch} rates and lower N_V for $\overline{T}$ 1285°C and 72 min period (Fig. 11) drastically reduce the amount of existing crystals due to long periods of dissolution at near liquidus temperatures (~1°C of undercooling). However, this does not occur in experiments with maximum temperatures (up-T cycle) 10°C below the liquidus (i.e. $\overline{T}$ 1265 and 1275°C). $^{50}G_{max}$ and $^{50}A_{max}^{0.5}$ values for the same experiments are lower at lower amounts of cycles (Fig. 13b, d) which suggests that unless a long enough time is spent at near-liquidus conditions, the number of cycles has more control on propagated crystal growth. Mills and Glazner (2013) also suggested that increased period could coarsen crystals by enhanced diffusion-controlled dissolution at near liquidus conditions.

Period is a function of frequency ($\tau = 1/F$) and it does not seem to play a large role in coarsening titanite. Rather, an increase in the number of cycles relative to time increases overall crystal sizes (Fig. 13b). Mills and Glazner (2013) similarly found period effects to be of second order compared to amplitude. For example, if a crystal-melt system spends long periods of time at near-liquidus conditions, regardless of the period, crystallization on the down-T portion of the cycle is controlled dominantly by the degree of undercooling, or the amplitude of the cycle.

CSD modeling

The cycled CSDs lower slopes relative to static and seeded CSDs, suggest a transfer of mass from small to large crystals (Fig. 14a, b, c). The break in slope for CSDs from $\overline{T}$ 1285°C with long periods (i.e., τ = 60, 72 min; Fig. 14c), resemble CSDs of an open system (Fig. 1a) measured by Higgins (1999). Higgins interpreted the steep sloped CSDs, of small crystal sizes

(Fig. 1a), as groundmass crystals formed from initial cooling of the magma. However, the existence of small crystal sizes (<50 μm) resulting from cycling (Fig. 14), shows that prolonged cooling is not necessary to form steep sloped CSDs. Thus, it is reasonable that small groundmass crystals can form from dynamic cycling rather than steady state cooling. Furthermore, CSDs of the same character may be formed by different processes, making them non-unique.

Experiments held at high and low-T instead of at the $\overline{T}$ for 30 min prior to quenching, show considerable variation from each other after only 4 cycles (3.2-h) (Fig. 14d). Titanite precipitated and coarsened crystals during down-T crystallization at a rate of 19°C/h, raising overall crystal sizes. The high-T quench run has smaller crystal sizes owing to titanite dissolution. Simakin and Bindeman (2008) theorized that cycling could coarsen populations after just one precipitation-dissolution event. However, at such short experiment durations, CSD slopes are not as shallow as the 50-h experiments (Fig. 14a, b, c), suggesting that repeated precipitation-dissolution events are important for developing mature textures.

CSDs are qualitatively influenced by coarsening of crystals from repeated intervals of increased undercooling, and periods of buffering close to the liquidus (Higgins, 1999). Higgins and Roberge (2003) described CSDs that rotate around a small crystal size as the combination of CN theoretical coarsening and increased nucleation density (Fig. 2b, c). During cycling, the net-effects of dissolution versus precipitation is greater for smaller crystals (i.e. they dissolve quicker than they can precipitate; Mills et al., 2011). Unless two crystals coalesce to form a larger one, growth is greater for larger crystals during down-T crystallization, effectively buffering larger crystal sizes (Eberl et al., 2002). If nucleation is suppressed during closed system (batch) thermal cycling, the existence of surviving small crystals must be relicts (Mills et al. 2011). Therefore,

batch thermal cycling will retain smaller sizes because of limitations on nucleation rates, crystal solute in the melt, the amount of oscillations, and the degree of undercooling.

Implications for titanite growth in igneous systems

Temperature oscillations within a magma body complicate classic igneous texture interpretations. For example, crystals that are large and well-formed (euhedral), were thought to form early in large melt fractions with a constant crystallization sequence (Bryon et al., 1995). Frost et al. (2000) suggested that igneous titanite crystallizes above its closure temperature of >700°C (Hayden et al., 2008). However, phase equilibria of titanite in silicic magmas are poorly understood and there are few quantitative constraints on its stability (Colombini et al., 2011; Glazner et al, 2008). Colombini et al. (2011) attributed the high abundance of titanite in the intermediate composition Searchlight pluton of southern Nevada to late-stage crystallization of titanite in highly silicic, evolved pockets of melt. Other studies of granitoids reveal histories of incremental emplacement based on pluton compositional zoning, thermochronologic data, and zircon dating (Coleman et al., 2004; Johnson and Glazner, 2010; Davis et al., 2012; Frazer et al., 2014). Repeated thermal oscillations with temperatures varying by at least 10°C and repeated buffering close to the titanite liquidus, could cause titanite trapped in melt pockets to mature into euhedral crystals (Coleman et al., 2012). Thermal cycling effects complicate crystal nucleation and growth with disequilibrium overprint of otherwise equilibrium conditions that can falsely represent crystallization conditions and final resting states. Mature igneous textures may not represent indiscriminant processes because crystal growth from thermal cycling satisfies other CSD coarsening models (e.g. Higgins, 1999).

Igneous titanite often displays REE oscillatory and sector zoning (Paterson and Stephens, 1992; Frost et al., 2000). REE oscillatory zoning of titanite in the Half Dome granodiorite,

California, did not represent equilibrium conditions and could have been caused by fluctuating partition coefficients induced by fresh magmatic influxes and fluctuating temperatures (Bauer, 2015). Hayden et al. (2008) found sector zoning of Zr in synthetically grown titanite used for Zr-in-titanite analysis but neglected enriched Zr zones from the crystallization thermometer because they overestimated temperatures by ~48-70°C which did not represent equilibrium concentrations. Glazner and Johnson (2013) challenged the use of Zr-in-titanite thermometer in titanite inclusions within K-feldspar from megacrystic granites, arguing that repeated fluxing of hot fluids could change REE, Fe, and Al contents that could cumulatively affect calculated temperatures. Oscillatory zoning, while not observed in the homogenous titanite of this study, could be caused by oscillating temperatures. Furthermore, titanite's euhedral form is favorable in most of our thermal cycling conditions and possibly other phases easily achieve mature form by thermal cycling conditions (Erdman and Koepke, 2016; Wu et al., 2016).

CONCLUSIONS

Experiments involving disequilibrium environments such as thermal cycling are needed to understand the growth of crystals comprising igneous textures. We conclude from this study that:

1. Nucleation is suppressed during thermal cycles due to heterogeneous nucleation on existing crystals. G_{batch} values are highly dependent on the density of a crystal population and should be considered an evaluation of nucleation rate.
2. Growth effects of thermal cycling in homogeneous batch crystal-melt systems are predominantly controlled by the amplitude of the cycle.
3. Repeated thermal oscillations increase crystal size and growth rate but the length of period does not directly affect crystal growth. However, if sufficiently long periods and near-liquidus temperatures are achieved, crystal populations will consist of a small number of large crystals.
4. CSDs created from different processes can have similar qualities, complicating classic interpretations of textures. Textural analysis continues to evolve but interpretation of CSDs may confuse processes leading to misinterpretations of natural mature igneous textures.
5. Titanite in natural systems that exhibits oscillatory zoning and larger euhedral sizes may have been subject to repeated intensive variable changes such as thermal cycling during crystallization. Chemical and compositional studies should be reconsidered to involve more dynamic and disequilibrium environments.

APPENDIX A: COMPOSITION OF NATURAL STARTING MATERIALS

oxide	Albite: Morefield Mine, Virginia	Titanite: Delicias Mine, Ensenada, Baja California
Na_2O	10.71	0
MgO	0.07	0.1
Al_2O_3	20.74	0.98
SiO_2	66.72	31.06
P_2O_5	-0.04	0.12
K_2O	0.8	0.06
CaO	0.93	28.9
TiO_2	0.02	37.39
MnO	0.005	0.057
Fe_2O_3	0.03	0.94
total	99.98	99.61

Note: Analysis was done using a XRF system

REFERENCES

Bachmann, O., & Bergantz, G. W. (2008). Rhyolites and their source mushes across tectonic settings. *Journal of Petrology*, *49*(12), 2277–2285.

Bateman, P., & Chappell, B. (1979). Crystallization, fractionation , and solidification of the Intrusive Series , Yosemite National Park , California. *Geological Society of America Bulletin*, *90*, 465–482.

Bauer, J. (2015). Complex zoning patterns and rare earth element variations across titanite crystals from the Half Dome Granodiorite, Central Sierra Nevada, California. *[Master's Thesis]: University of North Carolina, Chapel Hill*, 76.

Blundy, J., & Cashman, K. (2008). Petrologic reconstruction of magmatic system variables and processes. *Reviews in Mineralogy and Geochemistry*, *69*(1), 179–239.

Bryon, D. N., Atherton, M., & Hunter, R. (1995). The interpretation of granitic textures from serial thin sectioning, image analysis and three-dimensional reconstruction. *Mineralogical Magazine*, *59*(395), 203–211.

Cabane, H., Laporte, D., & Provost, A. (2001). Experimental investigation of the kinetics of Ostwald ripening of quartz in silicic melts. *Contributions to Mineralogy and Petrology*, *142*(3), 361–373.

Cabane, H., Laporte, D., & Provost, A. (2005). An experimental study of Ostwald ripening of olivine and plagioclase in silicate melts: Implications for the growth and size of crystals in magmas. *Contributions to Mineralogy and Petrology*, *150*(1), 37–53.

Carmichael, I. S., Turner, F. J., & Verhoogen, J. (1974). Igneous petrology. *McGraw-Hill*, 739.

Cashman, K. V., & Marsh, B. D. (1988). Crystal size distribution (CSD) in rocks and the kinetics and dynamics of crystallisation. *Contributions to Mineralogy and Petrology*, *99*, 292–305.

Cherniak, D. J. (2006). Zr diffusion in titanite. *Contributions to Mineralogy and Petrology*, *152*(5), 639–647.

Coleman, D. S., Bartley, J. M., Glazner, A. F., & Pardue, M. J. (2012). Is chemical zonation in plutonic rocks driven by changes in source magma composition or shallow-crustal differentiation ?, (6), 1568–1587.

Coleman, D. S., Gray, W., & Glazner, A. F. (2004). Rethinking the emplacement and evolution of zoned plutons: Geochronologic evidence for incremental assembly of the Tuolumne Intrusive Suite, California. *Geology*, *32*(5), 433–436.

Colombini, L. L., Miller, C. F., Gualda, G. A. R., Wooden, J. L., & Miller, J. S. (2011). Sphene and zircon in the Highland Range volcanic sequence (Miocene, southern Nevada, USA):

Elemental partitioning, phase relations, and influence on evolution of silicic magma. *Mineralogy and Petrology*, *102*(1-4), 29–50.

Davis, J. W., Coleman, D. S., Gracely, J. T., Gaschnig, R., & Stearns, M. (2012). Magma accumulation rates and thermal histories of plutons of the Sierra Nevada batholith, CA. *Contributions to Mineralogy and Petrology*, *163*(3), 449–465.

Donaldson, C. H. (1976). An experimental investigation of olivine morphology. *Contributions to Mineralogy and Petrology*, *57*(2), 187–213.

Donhowe, D. P., & Hartel, R. W. (1996). Recrystallization of ice in ice cream during controlled accelerated storage. *International Dairy Journal*, *6*(11), 1191–1208.

Eberl, D. D., Drits, V. a, & Srodon, J. (2001). User's Guide to Galoper: A Program for Simulating the Shapes of Crystal Size Distributions from Growth Mechanisms and Associated Programs. *U.S. Geological Survey Open-File Report OF00-505*, 1–44.

Eberl, D., Kile, D., & Drits, V. (2002). On geological interpretations of crystal size distributions: Constant vs. proportionate growth. *American Mineralogist*, *87*, 1235–1241.

Erdman, M., & Koepke, J. (2016). Experimental temperature cycling as a powerful tool to enlarge melt pools and crystals at magma storage conditions, *American Mineralogist*, *101*, 960–969.

Frazer, R. E., Coleman, D. S., & Mills, R. (2014). Zircon U-Pb geochronology of the Mount Givens Granodiorite: Implications for the genesis of large volumes of eruptible magma. *Journal of Geophysical Research: Solid Earth*, *119*, 2907–2924.

Frost, B. R., Chamberlain, K. R., & Schumacher, J. C. (2001). Sphene (titanite): Phase relations and role as a geochronometer. *Chemical Geology*, *172*(1-2), 131–148.

Girolami, M. W., & Rousseau, R. W. (1985). Size--Dependent Crystal Growth-A Manifestation of Growth Rate Dispersion in the Potassium Alum--Water System. *AIChE Journal*, *31*(11), 1821–1828.

Glazner, a. F., & Mills, R. D. (2012). Interpreting two-dimensional cuts through broken geologic objects: Fractal and non-fractal size distributions. *Geosphere*, *8*(4), 902–914.

Glazner, A. F., Coleman, D. S., & Bartley, J. M. (2008). The tenuous connection between high-silica rhyolites and granodiorite plutons. *Geology*, *36*(2), 183.

Glazner, A. F., & Johnson, B. R. (2013). Late crystallization of K-feldspar and the paradox of megacrystic granites. *Contributions to Mineralogy and Petrology*, *166*(3), 777–799.

Hammer, J. E., & Rutherford, M. J. (2002). An experimental study of the kinetics of decompression-induced crystallization in silicic melt. *Journal of Geophysical Research*,

107(B1).

Harper, B. E., Miller, C. F., Koteas, G. C., Gates, N. L., Wiebe, R. A., Lazzareschi, D. S., & Cribb, J. W. (2004). Granites , dynamic magma chamber processes and pluton construction : the Aztec Wash pluton, Eldorado Mountains, Nevada, USA. *Transactions of the Royal Society of Edinburgh: Earth Sciences*, *95*, 277–295.

Hayden, L. A., Watson, E. B., & Wark, D. A. (2008). A thermobarometer for sphene (titanite). *Contributions to Mineralogy and Petrology*, *155*(4), 529–540.

Hersum, T. G., & Marsh, B. D. (2007). Igneous textures: On the kinetics behind the words. *Elements*, *3*(4), 247–252.

Higgins, M. D. (1998). Origin of Anorthosite by Textural Coarsening: Quantitative Measurements of a Natural Sequence of Textural Development. *Journal of Petrology*, *39*(7), 1307–1323.

Higgins, M. D. (2000). Measurement of crystal size distributions. *American Mineralogist*, *85*, 1105–1116.

Higgins, M. D. (2002). A crystal size-distribution study of the Kiglapait layered mafic intrusion , Labrador, Canada: evidence for textural coarsening. *Contributions to Mineralogy and Petrology*, *144*, 314–330.

Higgins, M. D. (2006). Quantitative textural measurements in igneous and metamorphic petrology. *Cambridge University Press.*

Higgins, M. D. (2011). Quantitative petrological evidence for the origin of K-feldspar megacrysts in dacites from Taapaca volcano, Chile. *Contributions to Mineralogy and Petrology*, *162*(4), 709–723.

Higgins, M. D., & Roberge, J. (2003). Crystal Size Distribution of Plagioclase and Amphibole from Soufriere Hills Volcano, Montserrat: Evidence for Dynamic Crystallization-Textural Coarsening Cycles. *Journal of Petrology*, *44*(8), 1401–1411.

Hintzmann, W., & Müller-Vogt., G. (1969). Crystal growth and lattice parameters of rare-earth doped yttrium phosphate, arsenate and vanadate prepared by the oscillating temperature flux technique. *Journal of Crystal Growth*, *5*, 274–278.

Huppert, H. E., & Sparks, R. S. J. (1988). The Generation of Granitic Magmas by Intrusion of Basalt into Continental Crust. *Journal of Petrology*, *29*(3), 599–624.

Jerram, D. A., & Davidson, J. P. (2007). Frontiers in textural and microgeochemical analysis. *Elements*, *3*, 235–238.

Johnson, B. R., & Glazner, A. F. (2010). Formation of K-feldspar megacrysts in granodioritic

plutons by thermal cycling and late-stage textural coarsening. *Contributions to Mineralogy and Petrology*, *159*(5), 599–619.

Kirkpatrick, J. R. (1977). Nucleation and growth of plagioclase, Makaopuhi and Alae lava lakes, Kilauea Volcano, Hawaii. *Geological Society of America Bulletin,* (88), 78-84.

Lasaga, A. C. (1998). *Reaction Kinetics in Geoscience*. *Princeton University Press, Princeton*.

Lofgren, G. (1974). An experimental study of plagioclase crystal morphology: isothermal crystallization. *American Journal of Science*, *274*(3), 243–273.

Lofgren, G. E. (1980). Experimental studies on the dynamic crystallization of silicate melts, *in* Hargraves, R.B., ed., Physics of Magmatic Processes: Princeton, N.J., Princeton University Press, p. 487-551.

Loomis, T. P. (1982). Numerical simulations of crystallization processes of plagioclase in complex melts: the origin of major and oscillatory zoning in plagioclase. *Contributions to Mineralogy and Petrology*, *81*(3), 219–229.

Marsh, B. (1998). On the interpretation of crystal size distributions in magmatic systems. *Journal of Petrology*, *39*(4), 553–599.

Marsh, B. D. (1988). Crystal size distribution (CSD) in rocks and the kinetics and dynamics of crystallisation. *Contributions to Mineralogy and Petrology*, *99*, 277–291.

Mills, R. D., Ratner, J. J., & Glazner, a. F. (2011). Experimental evidence for crystal coarsening and fabric development during temperature cycling. *Geology*, *39*(12), 1139–1142.

Mills, R., & Glazner, A. (2013). Experimental study on the effects of temperature cycling on coarsening of plagioclase and olivine in an alkali basalt. *Contributions to Mineralogy and Petrology*, *166*(1), 97–111.

Morgan, D. J., & Jerram, D. A. (2006). On estimating crystal shape for crystal size distribution analysis. *Journal of Volcanology and Geothermal Research*, *154*(1-2), 1–7.

Nemchin, A. A., Giannini, L. M., Bodorkos, S., & Oliver, N. H. S. (2001). Ostwald ripening as a possible mechanism for zircon overgrowth formation during anatexis: Theoretical constraints, a numerical model, and its application to pelitic migmatites of the tickalara metamorphics, Northwestern Australia. *Geochimica et Cosmochimica Acta*, *65*(16), 2771–2787.

Paque, J. M., Lofgren, G. E., & Le, L. (2000). Crystallization of calcium-aluminium-rich inclusions: Experimental studies on the effects of repeated heating events. *Meteoritics & Planetary Sciences*, *35*, 363–371.

Paterson, B. A., & Stephens, W. E. (1992). Kinetically induced compositional zoning in titanite:

implications for accessory-phase/melt partitioning of trace elements. *Contributions to Mineralogy and Petrology*, *109*(3), 373–385.

Peter Gromet, L., & Silver, L. T. (1983). Rare earth element distributions among minerals in a granodiorite and their petrogenetic implications. *Geochimica et Cosmochimica Acta*, *47*(5), 925–939.

Pupier, E., Duchene, S., & Toplis, M. J. (2008). Experimental quantification of plagioclase crystal size distribution during cooling of a basaltic liquid. *Contributions to Mineralogy and Petrology*, *155*(5), 555–570.

Samperton, K. M., Schoene, B., Cottle, J. M., Keller, C. B., Crowley, J. L., Schmitz, M. D. (2015). Magma emplacement, differentiation and cooling in the middle crust: Integrated zircon geochronological–geochemical constraints from the Bergell Intrusion, Central Alps. *Chemical Geology*, 417, 322-340.

Scheel, H. J., & Elwell, D. (1972). Stable growth rates and temperature programming in flux growth. *Journal of Crystal Growth*, *12*, 153–161.

Schiavi, F., Walte, N., & Keppler, H. (2009). First in situ observation of crystallization processes in a basaltic-andesitic melt with the moissanite cell. *Geology*, *37*(11), 963–966.

Underwood, E. E. (1970). Quantitative stereology. *Addison-Wesley, Massechussetts*.

Verhoogen, J. (1962). Distribution of titanium between silicates and oxides in igneous rocks. *American Journal of Science*, *260*, 211–220.

Voorhees, P. W. (1985). The theory of Ostwald ripening. *Journal of Statistical Physics*, *38*(1-2), 231–252.

Watson, E.B. (1982). Basalt contamination by continental crust: Some experiments and models. *Contributions to Mineralogy and Petrology.* (80), 73-87.

Wu, Z., Yang, S., & Wu, W. (2016). Application of temperature cycling for crystal quality control during crystallization. *CrystEngComm*.

Wyllie, P. J., Cox, K. G., & Biggar, G. M. (1962). The habit of apatite in synthetic systems and igneous rocks. *Journal of Petrology*, *3*(2), 238–243.

Zieg, M. J., & Lofgren, G. E. (2006). An experimental investigation of texture evolution during continuous cooling. *Journal of Volcanology and Geothermal Research*, *154*(1-2), 74–88.